New effective interaction for *pf*-shell nuclei and its implications for the stability of the $N=Z=28$ closed core

M. Honma,[1] T. Otsuka,[2,3] B. A. Brown,[4] and T. Mizusaki[5]
[1]*Center for Mathematical Sciences, University of Aizu, Tsuruga, Ikki-machi, Aizu-Wakamatsu, Fukushima 965-8580, Japan*
[2]*Department of Physics and Center for Nuclear Study, University of Tokyo, Hongo, Tokyo 113-0033, Japan*
[3]*RIKEN, Hirosawa, Wako-shi, Saitama 351-0198, Japan*
[4]*National Superconducting Cyclotron Laboratory and Department of Physics and Astronomy, Michigan State University, East Lansing, Michigan 48824-1321, USA*
[5]*Institute of Natural Sciences, Senshu University, Higashimita, Tama, Kawasaki, Kanagawa 214-8580, Japan*
(Received 20 November 2003; published 29 March 2004)

The effective interaction GXPF1 for shell-model calculations in the full *pf* shell is tested in detail from various viewpoints such as binding energies, electromagnetic moments and transitions, and excitation spectra. The semimagic structure is successfully described for N or $Z=28$ nuclei, ^{53}Mn, ^{54}Fe, ^{55}Co, and ^{56,57,58,59}Ni, suggesting the existence of significant core excitations in low-lying nonyrast states as well as in high spin yrast states. The results of $N=Z$ odd-odd nuclei, ^{54}Co and ^{58}Cu, also confirm the reliability of GXPF1 interaction in the isospin dependent properties. Studies of shape coexistence suggest an advantage of Monte Carlo shell model over conventional calculations in cases where full-space calculations still remain too large to be practical.

DOI: 10.1103/PhysRevC.69.034335 PACS number(s): 21.60.Cs, 21.30.Fe, 27.40.+z, 27.50.+e

I. INTRODUCTION

The effective interaction is a key ingredient for the success of the nuclear shell model. Once a reliable interaction is obtained, we can describe various nuclear properties accurately and systematically, which helps us to understand the underlying structure, and to make predictions for unobserved properties. The *pf* shell for orbitals $1p_{3/2}$, $1p_{1/2}$, $0f_{7/2}$, and $0f_{5/2}$ is a region where the shell model can play an indispensable role, and is at the frontier of our computational abilities. In the *pf* shell one finds the interplay of collective and single-particle properties, both of which the shell model can describe within a unified framework. Since the protons and neutrons occupy the same major shell, the proton-neutron interaction is relatively strong and one can study related collective effects such as $T=0$ pairing. The *pf*-shell nuclei are also of special interest from the viewpoint of astrophysics, such as the electron capture rate in supernovae explosions. For all these applications, a suitable effective interaction for *pf*-shell nuclei is required.

Because of the spin-orbit splitting, there is a sizable energy gap between the $f_{7/2}$ orbit and the other three orbits $(p_{3/2},p_{1/2},f_{5/2})$. Thus there exists an N or $Z=28$ "magic" number inside the major shell with the oscillator quantum number $N_{\rm osc}=3$. For shell-model calculations around this magic number, ^{56}Ni has often been assumed as an "inert" core. However, it has been shown that this core is rather soft [1] and the closed-shell model for the magic number 28 provides a very limited description especially for nuclei near N or $Z=28$ semimagic. This "active-two-shell" problem is a challenge to both nuclear models and effective interactions. We shall discuss this point in this paper, and the word "cross-shell" refers to the N or $Z=28$ shell gap hereafter. Because of such cross-shell mixing, it is necessary to assume essentially the full set of *pf* configurations and the associated unified interaction in order to describe the complete set of data and to have some predictive power.

The effective interaction can in principle be derived from the free nucleon-nucleon interaction. In fact such microscopic interactions have been proposed for the *pf* shell [2,3] with certain success particularly in the beginning of the shell. These interactions, however, fail in cases of many valence nucleons, e.g., ^{48}Ca [3,4] and ^{56}Ni. Especially in the latter, the ground state is predicted to be significantly deformed in the full *pf*-shell calculation, contrary to its known double-magic structure.

It has been shown that modifications in the monopole part of the microscopic interaction can greatly improve the description of experimental data. In fact, KB3 [5] and KB3G [6] interactions, which were obtained on the basis of the microscopic Kuo-Brown's G-matrix interaction [2] with various monopole corrections, are remarkably successful for describing lighter *pf*-shell nuclei ($A\leqslant 52$). However, as we have pointed out [7], these interactions fail near ^{56}Ni. Therefore it is interesting to investigate to what extent the monopole modification is useful as a simple recipe for improvement of the microscopic interaction and to what extent one has to go beyond this.

One feasible way of modifying the microscopic interaction for practical use is to carry out an empirical fit to a sufficiently large body of experimental energy data. In fact such a method has been successfully applied to lighter nuclei and has resulted in the "standard" effective interactions of Cohen-Kurath [8] and USD [9] for the *p* and *sd* shells, respectively.

Along this line, we have recently developed a new effective interaction called GXPF1 [7] for use in the *pf* shell. Starting from a microscopic interaction, a subset of the 195 two-body matrix elements and four single-particle energies are determined by fitting to 699 energy data in the mass

range $A=47-66$. It has already been shown that GXPF1 successfully describes energy levels of various *pf*-shell nuclei, such as the first 2^+ states in even-even $Z\leqslant 28$ isotopes, low-lying states of ^{56,57,58}Ni, and the systematics of the yrast $1/2^-$, $3/2^-$, and $5/2^-$ states in Ni isotopes [7]. Therefore it is now important to analyze the wave functions and examine some electromagnetic properties to confirm further the reliability of the interaction.

The aim of this paper is to present various results predicted by GXPF1 in order to clarify its applicability and limitation by comparing these results with experimental data. We also discuss what modifications of the microscopic interaction are needed in addition to the monopole corrections in order to obtain a better description of nuclear properties over the wide range of nuclei in the *pf* shell.

In the derivation and previous tests of GXPF1, the Monte Carlo shell model (MCSM) [1,10] played a crucial role, since at that time it was the only feasible way to obtain shell-model eigenenergies for many states in the middle of the *pf* shell. On the other hand, in the present paper, most of the results have been obtained by the conventional Lanczos diagonalization method, which is now feasible with reasonable accuracy for most *pf*-shell nuclei owing to recent developments of an efficient shell-model code and fast computers. We will confirm our previous MCSM results by comparison with those by such conventional calculations, but there are still places where the MCSM is necessary. The *pf* shell is the current frontier of conventional methods, while the MCSM is applicable and useful in much larger model spaces, as demonstrated in Refs. [11–14].

This paper is organized as follows. In Sec. II, the derivation of GXPF1 is reviewed and its general properties are analyzed in some detail. In Sec. III experimental data are compared with the results of large-scale shell-model calculations based on GXPF1 and some of its possible modifications. We analyze the structure of wave functions focusing on the core-excitations across the N or $Z=28$ shell gap. A summary is given in Sec. IV.

II. DERIVATION AND PROPERTIES OF THE EFFECTIVE INTERACTION

In this section, we first sketch how we have derived the GXPF1 interaction. The properties of GXPF1 are then analyzed from various viewpoints.

A. Derivation of GXPF1 interaction

An effective interaction for the *pf* shell can be specified uniquely in terms of interaction parameters consisting of four single-particle energies ϵ_a and 195 two-body matrix elements $V(abcd;JT)$, where $a,b,\ldots$ denote single-particle orbits, and JT stand for the spin-isospin quantum numbers. ϵ_a's include kinetic energies. We take the traditional approach of evaluating the interaction energy in zeroth-order perturbation theory for n nucleons outside of a closed shell for ^{40}Ca. We adjust the values of the interaction parameters so as to fit experimental binding energies and energy levels. We outline the fitting procedure here, while details can be found in Ref. [15]. For a set of N experimental energy data $E^k_{\rm expt}(k=1,\ldots,N)$, we calculate the corresponding shell-model eigenvalues λ_k's. We minimize the quantity $\chi^2=\Sigma^N_{k=1}(E^k_{\rm expt}-\lambda_k)^2$ by varying the values of the interaction parameters. Since this minimization is a nonlinear process with respect to the interaction parameters, we solve it in an iterative way with successive variations of those parameters followed by diagonalizations of the Hamiltonian until convergence.

Experimental energies used for the fit are limited to those of ground and low-lying states. Therefore, certain linear combinations (LC's) of interaction parameters are sensitive to those data and can be well determined, whereas the rest of the LC's are not. We then adopt the so-called LC method [16], where the well-determined LC's are separated from the rest: starting from an initial interaction, well-determined LC's are optimized by the fit, while the other LC's are kept unchanged (fixed to the values given by the initial interaction).

In order to obtain shell-model energies, both the conventional and MCSM calculations are used. Since we are dealing with global features of the low-lying spectra for essentially all *pf*-shell nuclei, we use a simplified version of MCSM: we search for a few (typically three) most important basis states (deformed Slater determinants) for each spin-parity, and diagonalize the Hamiltonian matrix in the subspace spanned by these bases. The energy eigenvalues are improved by assuming an empirical correction formula, which is determined so that it reproduces the results of more accurate calculations for available cases. This method, the few-dimensional approximation with empirical corrections (FDA*), actually yields a reasonable estimate of the energy eigenvalues with much shorter computer time.

In the selection of experimental data for the fitting calculation, in order to eliminate intruder states from outside the present model space, we consider nuclei with $A\geqslant 47$ and $Z\leqslant 32$. As a result 699 data for binding and excitation energies (490 yrast, 198 yrare, and 11 higher states) were taken from 87 nuclei: $^{47-51}$Ca, $^{47-52}$Sc, $^{47-52}$Ti, $^{47-53,55}$V, $^{48-56}$Cr, $^{50-58}$Mn, $^{52-60}$Fe, $^{54-61}$Co, $^{56-66}$Ni, $^{58-63}$Cu, $^{60-64}$Zn, ^{62,64,65}Ga, and ^{64,65}Ge. We assume an empirical mass dependence $A^{-0.3}$ of the two-body matrix elements similar to that used for the USD interaction [9], which is meant to take into account the average mass dependence of a medium-range interaction [17]. We start from the microscopically derived effective interaction based on the Bonn-C potential [3], which is simply denoted by G hereafter. In the final fit, 70 well-determined LC's are varied, and a new interaction, GXPF1, was obtained with an estimated rms error of 168 keV within FDA*. The resultant single-particle energies and two-body matrix elements are listed in Table I.

B. Corrections to the microscopic interaction

It is interesting to examine what changes have been made to the original G interaction by the empirical fit. Figure 1 shows a comparison between GXPF1 and G for the 195 two-body matrix elements. One finds a strong correlation. On average, the $T=0$ ($T=1$) matrix elements are modified to be more attractive (repulsive). The most attractive matrix ele-

TABLE I. Two-body matrix elements $V(abcd;JT)$ (in MeV) of GXPF1 interaction. Single-particle energies are taken to be −8.6240, −5.6793, −1.3829, and −4.1370 MeV for the $f_{7/2}$, $p_{3/2}$, $f_{5/2}$, and $p_{1/2}$ orbit, respectively. For calculations of mass A nuclei, these two-body matrix elements should be multiplied by a factor $(A/42)^{-0.3}$.

$2j_a$	$2j_b$	$2j_c$	$2j_d$	J	T	V
7	7	7	7	1	0	−1.2838
7	7	7	7	3	0	−0.8418
7	7	7	7	5	0	−0.7839
7	7	7	7	7	0	−2.6661
7	7	7	3	3	0	−0.8807
7	7	7	3	5	0	−0.4265
7	7	7	5	1	0	1.8998
7	7	7	5	3	0	1.0917
7	7	7	5	5	0	1.2853
7	7	7	1	3	0	0.8883
7	7	3	3	1	0	−0.4313
7	7	3	3	3	0	−0.3415
7	7	3	5	1	0	−0.0907
7	7	3	5	3	0	0.0752
7	7	3	1	1	0	0.3150
7	7	5	5	1	0	0.6511
7	7	5	5	3	0	0.4358
7	7	5	5	5	0	0.1239
7	7	5	1	3	0	−0.1082
7	7	1	1	1	0	0.0271
7	3	7	3	2	0	−0.5391
7	3	7	3	3	0	−1.0055
7	3	7	3	4	0	−0.3695
7	3	7	3	5	0	−2.9670
7	3	7	5	2	0	−0.6381
7	3	7	5	3	0	0.2540
7	3	7	5	4	0	0.1951
7	3	7	5	5	0	0.6743
7	3	7	1	3	0	1.6850
7	3	7	1	4	0	0.1706
7	3	3	3	3	0	−0.4309
7	3	3	5	2	0	−1.2708
7	3	3	5	3	0	0.5790
7	3	3	5	4	0	−0.7103
7	3	3	1	2	0	−0.6228
7	3	5	5	3	0	0.1660
7	3	5	5	5	0	0.0334
7	3	5	1	2	0	1.0933
7	3	5	1	3	0	0.7227
7	5	7	5	1	0	−4.5802
7	5	7	5	2	0	−3.2520
7	5	7	5	3	0	−1.4019
7	5	7	5	4	0	−2.2583
7	5	7	5	5	0	−0.6084
7	5	7	5	6	0	−3.0351
7	5	7	1	3	0	−0.4252

TABLE I. (*Continued.*)

$2j_a$	$2j_b$	$2j_c$	$2j_d$	J	T	V
7	5	7	1	4	0	−0.3789
7	5	3	3	1	0	0.8914
7	5	3	3	3	0	0.6264
7	5	3	5	1	0	−1.2721
7	5	3	5	2	0	−0.5980
7	5	3	5	3	0	−0.7716
7	5	3	5	4	0	−0.6408
7	5	3	1	1	0	−1.4651
7	5	3	1	2	0	−0.7434
7	5	5	5	1	0	−0.2735
7	5	5	5	3	0	0.6378
7	5	5	5	5	0	1.1302
7	5	5	1	2	0	0.5447
7	5	5	1	3	0	0.6262
7	5	1	1	1	0	0.1928
7	1	7	1	3	0	−1.6968
7	1	7	1	4	0	−1.0602
7	1	3	3	3	0	0.6411
7	1	3	5	3	0	−0.0354
7	1	3	5	4	0	−1.3607
7	1	5	5	3	0	−0.2621
7	1	5	1	3	0	0.4505
3	3	3	3	1	0	−0.6308
3	3	3	3	3	0	−2.2890
3	3	3	5	1	0	0.2373
3	3	3	5	3	0	0.2276
3	3	3	1	1	0	1.8059
3	3	5	5	1	0	0.0483
3	3	5	5	3	0	−0.0546
3	3	5	1	3	0	0.1150
3	3	1	1	1	0	0.7675
3	5	3	5	1	0	−2.7262
3	5	3	5	2	0	−1.5110
3	5	3	5	3	0	−0.5859
3	5	3	5	4	0	−1.0882
3	5	3	1	1	0	−0.9930
3	5	3	1	2	0	−0.4885
3	5	5	5	1	0	0.4770
3	5	5	5	3	0	0.3200
3	5	5	1	2	0	0.3540
3	5	5	1	3	0	1.0151
3	5	1	1	1	0	0.8137
3	1	3	1	1	0	−2.5068
3	1	3	1	2	0	−2.3122
3	1	5	5	1	0	−0.0337
3	1	5	1	2	0	0.6900
3	1	1	1	1	0	0.8490
5	5	5	5	1	0	−0.8551

TABLE I. (*Continued.*)

$2j_a$	$2j_b$	$2j_c$	$2j_d$	J	T	V
5	5	5	5	3	0	−0.5599
5	5	5	5	5	0	−2.2816
5	5	5	1	3	0	−0.6276
5	5	1	1	1	0	−0.3161
5	1	5	1	2	0	−0.3174
5	1	5	1	3	0	−1.4023
1	1	1	1	1	0	−1.2431
7	7	7	7	0	1	−2.4385
7	7	7	7	2	1	−0.9352
7	7	7	7	4	1	−0.1296
7	7	7	7	6	1	0.2783
7	7	7	3	2	1	−0.5160
7	7	7	3	4	1	−0.2969
7	7	7	5	2	1	0.2167
7	7	7	5	4	1	−0.4999
7	7	7	5	6	1	−0.5643
7	7	7	1	4	1	−0.2096
7	7	3	3	0	1	−0.7174
7	7	3	3	2	1	−0.2021
7	7	3	5	2	1	−0.1725
7	7	3	5	4	1	−0.2224
7	7	3	1	2	1	−0.0367
7	7	5	5	0	1	−1.3832
7	7	5	5	2	1	−0.2038
7	7	5	5	4	1	−0.0331
7	7	5	1	2	1	−0.1295
7	7	1	1	0	1	−0.3800
7	3	7	3	2	1	−0.6081
7	3	7	3	3	1	0.1561
7	3	7	3	4	1	−0.1398
7	3	7	3	5	1	0.5918
7	3	7	5	2	1	0.0959
7	3	7	5	3	1	−0.5230
7	3	7	5	4	1	−0.2486
7	3	7	5	5	1	−0.4810
7	3	7	1	3	1	−0.1048
7	3	7	1	4	1	−0.3351
7	3	3	3	2	1	−0.3738
7	3	3	5	2	1	−0.5436
7	3	3	5	3	1	0.1836
7	3	3	5	4	1	−0.4546
7	3	3	1	2	1	−0.4262
7	3	5	5	2	1	0.0880
7	3	5	5	4	1	−0.2146
7	3	5	1	2	1	−0.8030
7	3	5	1	3	1	−0.1814
7	5	7	5	1	1	−0.0889
7	5	7	5	2	1	−0.1750

TABLE I. (*Continued.*)

$2j_a$	$2j_b$	$2j_c$	$2j_d$	J	T	V
7	5	7	5	3	1	0.6302
7	5	7	5	4	1	0.4763
7	5	7	5	5	1	0.7433
7	5	7	5	6	1	−0.9916
7	5	7	1	3	1	0.3224
7	5	7	1	4	1	0.1907
7	5	3	3	2	1	0.0717
7	5	3	5	1	1	0.0521
7	5	3	5	2	1	−0.4247
7	5	3	5	3	1	−0.0268
7	5	3	5	4	1	−0.2699
7	5	3	1	1	1	0.0552
7	5	3	1	2	1	−0.0153
7	5	5	5	2	1	−0.5022
7	5	5	5	4	1	−0.2709
7	5	5	1	2	1	−0.1537
7	5	5	1	3	1	0.1105
7	1	7	1	3	1	0.4873
7	1	7	1	4	1	−0.1347
7	1	3	5	3	1	0.3891
7	1	3	5	4	1	−0.6111
7	1	5	5	4	1	−0.2248
7	1	5	1	3	1	−0.1586
3	3	3	3	0	1	−1.1165
3	3	3	3	2	1	−0.0887
3	3	3	5	2	1	−0.4631
3	3	3	1	2	1	−0.6340
3	3	5	5	0	1	−1.2457
3	3	5	5	2	1	0.0719
3	3	5	1	2	1	−0.1923
3	3	1	1	0	1	−1.4928
3	5	3	5	1	1	0.3284
3	5	3	5	2	1	0.3608
3	5	3	5	3	1	0.3460
3	5	3	5	4	1	−0.2584
3	5	3	1	1	1	−0.1076
3	5	3	1	2	1	−0.4545
3	5	5	5	2	1	−0.0560
3	5	5	5	4	1	−0.3615
3	5	5	1	2	1	−0.4043
3	5	5	1	3	1	0.0600
3	1	3	1	1	1	−0.1594
3	1	3	1	2	1	−0.2938
3	1	5	5	2	1	0.0600
3	1	5	1	2	1	−0.2490
5	5	5	5	0	1	−1.2081
5	5	5	5	2	1	−0.4621
5	5	5	5	4	1	−0.1624

TABLE I. (*Continued.*)

$2j_a$	$2j_b$	$2j_c$	$2j_d$	J	T	V
5	5	5	1	2	1	−0.3208
5	5	1	1	0	1	−0.8093
5	1	5	1	2	1	−0.1519
5	1	5	1	3	1	0.2383
1	1	1	1	0	1	−0.4469

ments are $T=0$, with the largest ones belong to $T=0$ 7575 in both GXPF1 and G, as indicated in the figure, where the notation 7575 refers to the set of matrix elements $V(abab;JT)$ with $a=f_{7/2}$ and $b=f_{5/2}$. It was stressed in Refs. [18,19] that this strong $T=0$ interaction between the orbits $j_>=l+1/2$ and $j_<=l-1/2$ is an important feature in all mass regions including the *sd* and *p* shells. In the *p* shell variation of these type of matrix elements relative to the Cohen-Kurath interaction [8] leads to improvement [18,20]. One can see in Fig. 1 that the G and fitted (GXPF1) values for the $j_>$-$j_<$(7575) interactions are very similar.

There are seven matrix elements in which the difference between GXPF1 and G is greater than 500 keV. These matrix elements are listed in Table II. It is remarkable that these largely modified matrix elements are either of the diagonal $V(abab;JT)$ type which contributes to the monopole corrections or of the monopole pairing $(J=0,T=1)$ type. As for the former type, the 7373 and 7575, $T=0$ matrix elements with large J are modified to be more attractive, contrasting to the relatively small corrections for small J matrix elements. The two monopole pairing matrix elements shown in the table are both related to the $f_{5/2}$ orbit. As a result of the empirical fit, the pairing between $p_{3/2}$ and $f_{5/2}$ (3355) is modified to be strongly attractive, while that between $f_{7/2}$ and $f_{5/2}$ (7755) is made to be less attractive.

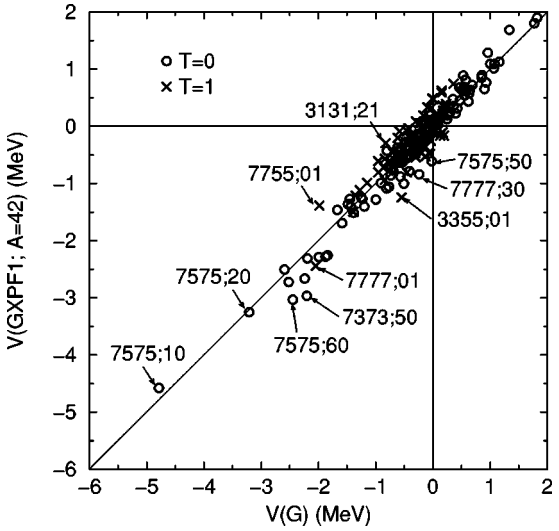

FIG. 1. Correlation of $V(abcd;JT)$ between G and GXPF1. The matrix elements of $T=0$ and $T=1$ are shown by open circles and crosses, respectively. For several matrix elements, corresponding quantum numbers are shown by using the notation $2j_a2j_b2j_c2j_d;JT$.

C. Monopole properties

In order to investigate basic properties of an effective Hamiltonian, it is convenient to decompose it into the monopole part and the multipole part [21] as

$$H = H_m + H_M. \tag{1}$$

The monopole part H_m plays a key role for describing bulk properties such as binding energies and shell gaps [5], since it determines the average energy of eigenstates in a given configuration. The monopole Hamiltonian is specified by the angular-momentum averaged two-body matrix elements:

$$V(ab;T) = \frac{\sum_J (2J+1)V(abab;JT)}{\sum_J (2J+1)}, \tag{2}$$

where the summations run over all Pauli-allowed values of the angular momentum J.

Figure 2 shows the matrix elements $V(ab;T)$. As a reference, we consider also the KB3G [6] interaction. Since this interaction gives an excellent description for $A\leqslant 52$ nuclei, it is expected that the monopole matrix elements of GXPF1 are similar to those of KB3G at least for those involving $f_{7/2}$. In fact, both $T=0$ and $T=1$ average matrix elements of the f7f7, f7p3, f7f5, and f7p1 orbit pairs are rather close between GXPF1 and KB3G. The $T=1$ matrix elements for p3p3, p3f5, and f5p1 are also not very different, which are important for describing $Z<28$, $N>28$ nuclei. On the other hand, the similarity is lost in other matrix elements, especially for $T=0$ matrix elements between $p_{3/2,1/2}$ orbits. Therefore, GXPF1 and KB3G could give a very different description for nuclei with $Z,N>28$.

In order to confirm this observation, we have carried out the FDA* calculations by using KB3G for the similar set of nuclei included in the fitting calculations. Table III summarizes the estimated rms difference between calculated energies and the experimental data for both GXPF1 and KB3G. The data are classified into four groups from the viewpoint of the location in the isotope table: (a) $Z,N<28$, (b) Z or $N=28$, (c) $Z<28$, $N>28$, and (d) $Z,N>28$. The rms deviations are estimated for each group, and the yrast and yrare states are considered separately.

It is clearly seen that the rms deviations by GXPF1 are almost the same in all groups. On the other hand, those by KB3G become larger for the group (b) and (d) in comparison to (a) and (c). The deviation is especially large for the group (b), where the major differences can be found in ^{56}Ni, ^{55}Co,

TABLE II. Comparison of the two-body matrix elements $V(abcd;JT)$ (MeV) ($A=42$) for which the difference between G and GXPF1 is larger than 500 keV.

$2j_a$	$2j_b$	$2j_c$	$2j_d$	J	T	G	GXPF1	Difference
7	3	7	3	5	0	−2.2033	−2.9670	−0.7637
3	3	5	5	0	1	−0.5457	−1.2457	−0.7000
7	7	7	7	3	0	−0.2404	−0.8418	−0.6014
7	5	7	5	6	0	−2.4425	−3.0351	−0.5926
7	5	7	5	5	0	−0.0211	−0.6084	−0.5873
3	1	3	1	2	1	−0.8291	−0.2938	+0.5353
7	7	5	5	0	1	−1.9875	−1.3832	+0.6043

and ^{57}Ni. Since the property of the core excitations appears directly in the low-lying spectra in these semimagic nuclei, this result suggests that the core excitations are not well described by the KB3G interaction.

The rms deviations are in general larger for yrare states than the yrast states, especially in KB3G. This also suggests the failure in the description of the core excitation, which is expected to appear more directly in the yrare states than the yrast states. Another possible reason is that the FDA* becomes less accurate for yrare states.

From this table we cannot infer that the description by GXPF1 is better than KB3G for group (a) and (c), because the rms deviations shown in the table are not exact values but the results of the FDA* with typical accuracy of about 200 keV. Since GXPF1 is determined from FDA*, the rms deviations of GXPF1 are naturally smaller than those by other interactions within the FDA*. In fact, in light *pf*-shell nuclei with more precise computations, we can find several examples where KB3G gives a better description than GXPF1.

D. Collective properties

It has been pointed out [21] that the multipole part of the Hamiltonian H_M is dominated by several terms, such as the pairing and the quadrupole-quadrupole interactions, which determine collective properties of the effective interaction. It is useful to investigate these collective aspects of GXPF1 and compare with that of other interactions.

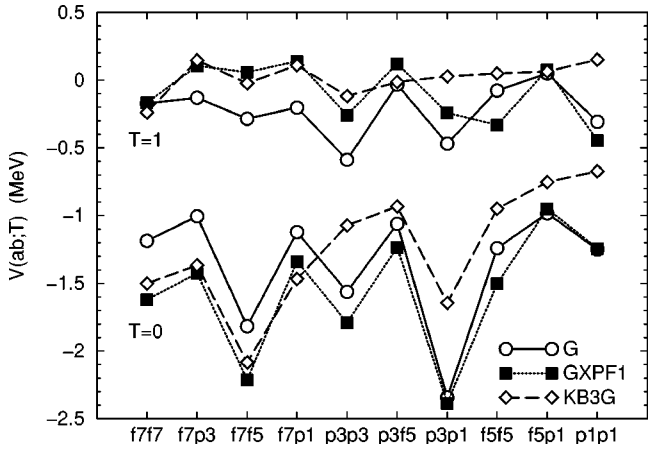

FIG. 2. Comparison of the monopole matrix elements $V(ab;T)$ ($A=42$) between G, GXPF1, and KB3G, which are shown by circles, squares, and diamonds, respectively. Lines are drawn to guide the eyes. The orbit-pair label "f5p3" stands for $a=f_{7/2}$ and $b=p_{3/2}$, for example.

According to the prescription in Ref. [21], H_M can be expressed in both the particle-particle (*p-p*) representation and the particle-hole (*p-h*) representation. In the *p-p* representation, H_M is expressed in terms of particle-pair bases $[c_a^\dagger c_b^\dagger]^{JT}$, in which two nucleons are coupled to the good angular momentum J and the isospin T. The coefficient matrix is diagonalized for each JT channel. By using the resultant eigenvalues E_α^{JT}, we obtain

$$H_M = \sum_{JT\alpha} E_\alpha^{JT} P_{JT\alpha}^\dagger P_{JT\alpha} + (\text{one-body terms}), \qquad (3)$$

where $P_{JT\alpha}^\dagger$ denote particle-pair creation operators which are linear combinations of the particle-pair bases, and their structure is determined by the corresponding eigenvectors. (Here, for simplicity, we omit the summations over z components of both spin and isospin.) The most important contributions come from the $JT=10$, 20, and 01 terms with large negative eigenvalues E^{JT}, which correspond to the $T=0$, small-J pairing, and the usual $T=1$ monopole pairing, respectively.

Similarly, in the *p-h* representation, by using the particle-hole (density) bases $[c_a^\dagger \tilde{c}_b]^{\lambda\tau}$ with spin-isospin quantum num-

TABLE III. Comparison of rms deviations (MeV) between the experimental excitation energies and those calculated from GXPF1 and KB3G. Theoretical energies are estimated by the FDA*. The numbers in the parentheses show the number of data included in the calculation.

Group	State	GXPF1	KB3G
(a) $Z,N<28$	Yrast	0.154(136)	0.235(129)
	Yrare	0.201(45)	0.263(23)
(b) Z or $N=28$	Yrast	0.184(92)	0.647(87)
	Yrare	0.195(57)	0.802(44)
(c) $Z<28$, $N>28$	Yrast	0.145(129)	0.296(126)
	Yrare	0.145(75)	0.302(55)
(d) $Z,N>28$	Yrast	0.186(55)	0.401(51)
	Yrare	0.187(23)	0.458(23)

TABLE IV. Comparison of the collective strengths (MeV) between G, GXPF1, and KB3G. The mass number $A=42$ is assumed.

Interaction	E^{01}	E^{10}	E^{20}	e^{20}	e^{40}	e^{11}
G	−4.20	−5.61	−2.96	−3.33	−1.30	+2.70
GXPF1	−4.18	−5.07	−2.85	−2.92	−1.39	+2.67
KB3G	−4.75	−4.46	−2.55	−2.79	−1.39	+2.47

bers $\lambda\tau$, the diagonalization of the coefficient matrix determines the structure of multipole operators $Q_{\lambda\pi k}$ and the corresponding strengths $e_k^{\lambda\tau}$, leading to an expression

$$H_M = \sum_{\lambda\pi k} e_k^{\lambda\tau} Q_{\lambda\pi k} \cdot Q_{\lambda\pi k}. \tag{4}$$

The symbol $\cdot$ stands for a scalar product with respect to both spin and isospin. [We adopt here a slightly different definition of $e_k^{\lambda\tau}$ from that in Ref. [21] by a phase factor $(-1)^{\lambda+\tau}$.] Large eigenvalues appear for $\lambda\tau=20$, 40, and 11, which are interpreted as the usual isoscalar quadrupole, hexadecapole, and Gamow-Teller interactions, respectively.

In Table IV, the collective strengths, i.e., the largest (smallest) eigenvalues E^{JT} or $e^{\lambda\tau}$ in each spin-isospin channel, are shown for G, GXPF1, and KB3G. According to the comparison between G and GXPF1, in general, the empirical fit has reduced these strengths by at most 12 % except for the $\lambda\tau=40$ term. Especially, the reductions in the $T=0$ terms E^{10} and e^{20} are relatively large, contrary to the general observation that $T=0$ matrix elements are on average modified to be more attractive by the empirical fit (see Fig. 1). This means that the attractive modification has been applied mainly to the monopole terms (which do not enter into the numbers of Table IV).

For the comparison between GXPF1 and KB3G, it can be seen that the $T=0$ ($T=1$) pairing strength is stronger (weaker) in GXPF1. Such a difference is expected to affect the description of the structure for $Z\sim N$ nuclei. In GXPF1, E^{10} is larger than E^{01} by about 20%, which is consistent with an estimate by the mean-field calculations [22] using the standard seniority pairing. It has also been shown [6] that the $T=0$ pairing strength is larger than $T=1$ in the density-dependent Gogny force. Note that the situation is opposite in KB3G. On the other hand, the multipole strengths $e^{\lambda\tau}$ are very similar for GXPF1 and KB3G, although the strengths of GXPF1 are slightly larger.

By using $e^{\lambda\tau}$, we can evaluate the collective quadrupole-quadrupole (QQ) strength between like nucleons (proton-proton or neutron-neutron) and that between protons and neutrons. For GXPF1, the strength of $Q_p\cdot Q_p$ or $Q_n\cdot Q_n$ is −0.96 MeV, while that of $Q_p\cdot Q_n$ is −7.82 MeV. This result shows the dominance of the proton-neutron part in the collective QQ interaction, as in heavier nuclei [14,23–25]. Such $Q_p\cdot Q_n$ dominance can be seen in other interactions, although the ratio of $Q_p\cdot Q_n$ to $Q_p\cdot Q_p$ (or $Q_n\cdot Q_n$) is different (8.1 for GXPF1, 6.8 for G, and 7.1 for KB3G).

E. Spin-tensor decomposition

In order to analyze the structure of an effective interaction, the spin-tensor decomposition [17] is useful, since it gives physical insights from a different viewpoint. In the following discussions, we consider the two-body interaction V_M in the multipole part H_M. Therefore the results are free from the monopole effects. We again take KB3G as a reference interaction. It is essentially the same as the Kuo-Brown's renormalized G-matrix interaction [2] after the monopole subtraction. (All of the results in this section are for the matrix elements evaluated at $A=42$.) An overview of the correlation in V_M between these interactions is shown in Fig. 3. It can be seen that the correction to the microscopic interaction imposed by an empirical fit contains sizable non-monopole components. In addition, the microscopic interactions, G and KB3G ($\sim$KB) are not identical even in the multipole parts, as seen in the lower part of Fig. 3. The difference between G and KB3G looks not necessarily smaller than that between G and GXPF1, which also suggests that the present correction to G is in a reasonable magnitude.

We first transform the *jj*-coupled two-body matrix elements $\langle j_a j_b JT|V_M|j_c j_d JT\rangle$ into the *LS*-coupled form $\langle l_a l_b LSJT|V_M|l_c l_d L'S'JT\rangle$, then carry out the spin-tensor decomposition of the two-body interaction as

$$V_M = \sum_k V_k = \sum_k U^k \cdot X^k, \tag{5}$$

where the operators U^k and X^k are irreducible tensors of rank k in the space and spin coordinates, respectively. The interaction components V_k represent the central ($k=0$), spin-orbit ($k=1$), and tensor ($k=2$) parts. The spin-orbit part includes both the normal part ($S=S'=1$) and the antisymmetric spin-orbit ($S\neq S'$) part.

Figure 4 shows the central components. For the $T=0$ matrix elements, G and GXPF1 are very similar to each other. Sizable modifications of G by the empirical fit can only be seen in the $(l_a l_b l_c l_d\, L)=(3333\ 0)$ and $(3131\ 2)$ components, which are made more repulsive by about 0.4 and 0.3 MeV, respectively. Other matrix elements of GXPF1 are very close to those of G. On the other hand, GXPF1 deviates from G in various $T=1$ matrix elements. The modifications to G are in the repulsive direction for the matrix elements (3333 0) and (3333 2) which are related to monopole and quadrupole pairing in the f orbit, respectively, while the (3311 0) matrix element is made to be more attractive, which corresponds to the monopole pairing between f and p orbits.

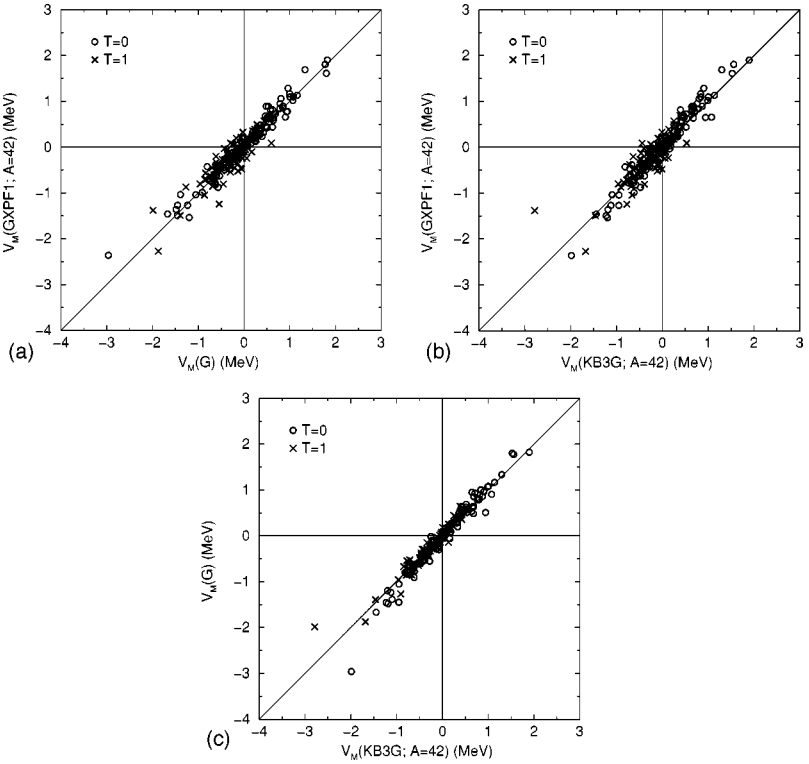

FIG. 3. Correlation of monopole-free two-body matrix elements V_M between (a) GXPF1 and G, (b) GXPF1 and KB3G, and (c) G and KB3G.

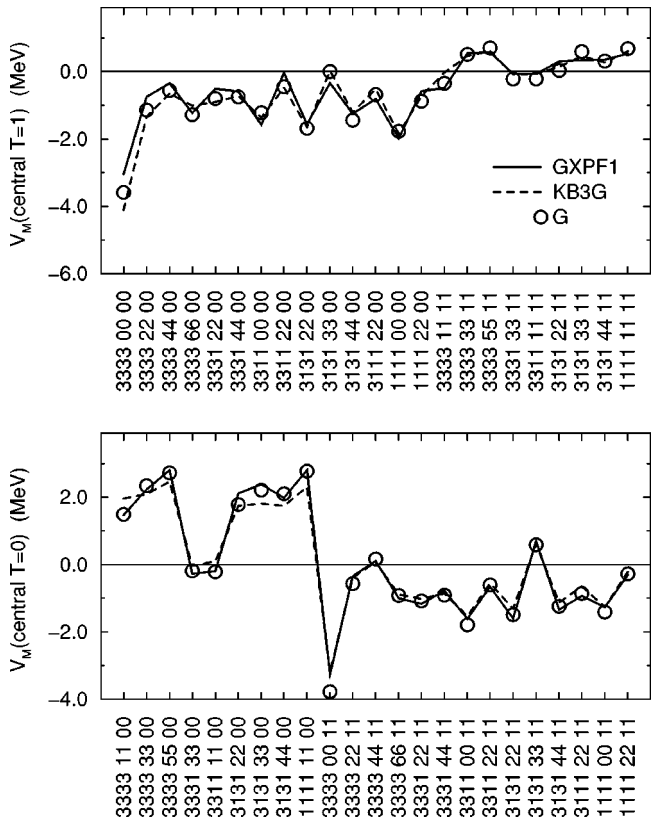

FIG. 4. Comparison of the central $T=0$ (lower panel) and $T=1$ (upper panel) components. Results for GXPF1, KB3G, and G are shown by solid lines, dotted lines, and circles, respectively. The quantum numbers $l_a l_b l_c l_d LL'SS'$ of the LS-coupled matrix elements $\langle l_a l_b LSJT|V|l_c l_d L'S'JT\rangle$ are shown along the horizontal axis.

For KB3G, it is remarkable that $T=0$, $S=1$ matrix elements are very close to those of GXPF1, including the (3333 0) matrix element which deviates from G significantly. Considering that the origin of KB3G and GXPF1 is very different, this similarity is surprising. However, there are large differences in the $T=0$, $S=0$ matrix elements, where the absolute values of the KB3G matrix elements are smaller in most cases than those of GXPF1 (and also G). The only exception is the (3333 1) matrix element. On the other hand, most of the $T=1$ matrix elements of KB3G are very close to those of G rather than GXPF1 for both $S=0$ and 1. One can only find small deviations from G in the (3333 0) and (3333 6) elements, where the former is more attractive and the latter is more repulsive. This similarity between G and KB3G indicates that the $T=1$ central part is converged in these two different G-matrix calculations.

In Fig. 5 the tensor components are compared. The $T=0$ matrix elements are relatively large for $\Delta L=2$. The corrections to G are relatively large for the $(l_a l_b l_c l_d\, LL')$ $=(3331\ 02)$, (3331 42), (3311 02), (3131 42), and (3111 42) matrix elements, which are all in the repulsive direction, while those in the attractive direction are found in (3333 64) and (3331 64) matrix elements. These corrections are at most 0.2 MeV. The $T=1$ components are in general very small compared to $T=0$. This is due to the fact that $T=0$ tensor interaction is dominated by a matrix element between two nucleons with $l=0$ to $l=2$ whereas $T=1$ must have odd l.

The G and KB3G values show rather large differences in cases with largest magnitudes, while the GXPF1 favors the G values with small corrections. Namely, in the $T=0$ cases, (3333 20), (3331 02), and (3111 20) matrix elements, the attraction of KB3G is much weaker, rather outstandingly, than that of G (and also GXPF1).

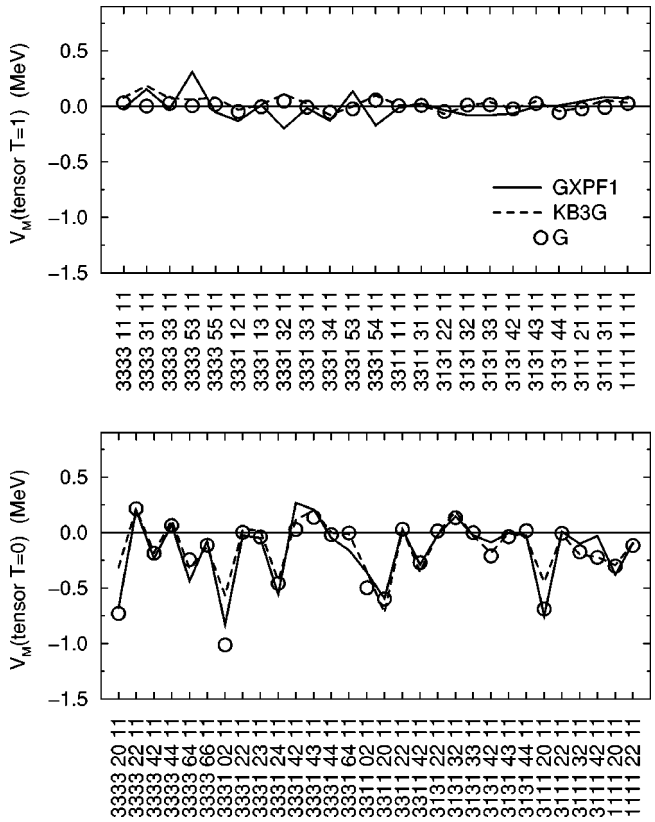

FIG. 5. Comparison of the tensor components. Conventions are the same as in Fig. 4.

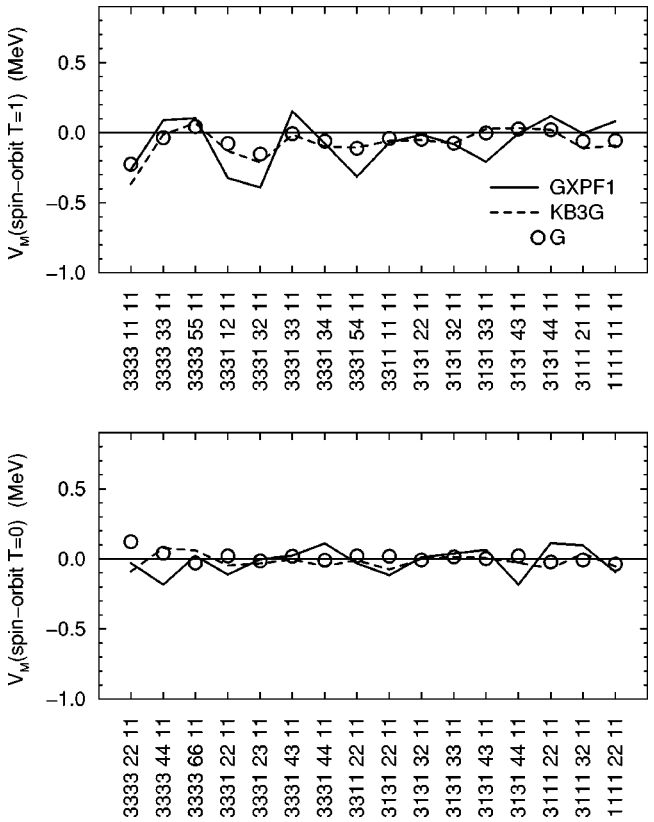

FIG. 6. Comparison of the spin-orbit components. Conventions are the same as in Fig. 4.

The normal spin-orbit components are shown in Fig. 6. For the $T=0$ elements, relatively large attractive corrections to G are found in the $(l_a l_b l_c l_d\, LL')=(3333\ 22)$, (3333 44), and (3131 44) matrix elements. Such corrections to the latter two matrix elements are not found in KB3G. Similarly, large attractive corrections exist also in the $T=1$, (3331 12), (3331 32), (3331 54), and (3131 33) matrix elements, all of which are absent in KB3G. It can be seen that the spin-orbit matrix elements of KB3G and G are very close in both cases of $T=0$ and 1. Thus, we infer that there may be contributions to the spin-orbit interaction that are not present in the two-nucleon G matrix, perhaps from an effective three-nucleon Hamiltonian.

Figure 7 shows the antisymmetric spin-orbit components. In general, matrix elements of G are small as in the case of the normal spin-orbit components. Nevertheless, one can again see nearly perfect similarity between G and KB3G in almost all matrix elements. The empirical fit has resulted in several large corrections to G which are inconsistent with KB3G, such as $T=0$, $(l_a l_b l_c l_d\, LL'\, SS')=(3331\ 32\ 01)$, (3331 54 01), (3331 44 10) and $T=1$, (3333 10 10), (3311 10 10), (3111 32 10). Such relatively large matrix elements appear also in other empirical effective interactions such as FPMI3 [26] and TBLC8 [27]. Further investigation is needed to find if these deviations are significant in terms of the errors inherent in the fits to data.

Summarizing the results of the spin-tensor decomposition of V_M, there are overall, reasonably good similarities between G and GXPF1 in relatively large matrix elements such as the central and the $T=0$ tensor components. The corrections due to the empirical fit become sizable in several specific matrix elements, especially for $T=1$. On the other hand, although many of matrix elements of KB3G are very close to those of G, one sees that several $T=S=0$ central and $T=0$ tensor matrix elements are rather different. This suggests significant changes in microscopic calculations of the effective interaction or their input from the nucleon-nucleon interaction that have evolved from the original calculations of Kuo-Brown to the more recent results of Ref. [3].

F. Monopole fit

According to previous sections, the empirical fit gives rise to sizable corrections to the microscopic interactions mostly in the monopole part and several specific matrix elements such as the monopole pairing. Therefore we come to a natural question: to what extent can we improve the microscopic interaction for practical use with more restrictive corrections. In order to assess this approach, we have carried out another fit by varying only the monopole parts, and the monopole-pairing $(T=1, J=0)$ and quadrupole-pairing $(T=1, J=2)$ matrix elements. The number of parameters are 20, 10, and 36 for these components, respectively. Thus in total 70 parameters are varied including four single-particle energies. Note that the $T=0$ components are varied only in the monopole part. The mass dependence $A^{-0.3}$ is also assumed. In the final fit, 45 best-determined LC's are taken, and the resultant interaction is referred to as GXPFM. The estimated rms devia-

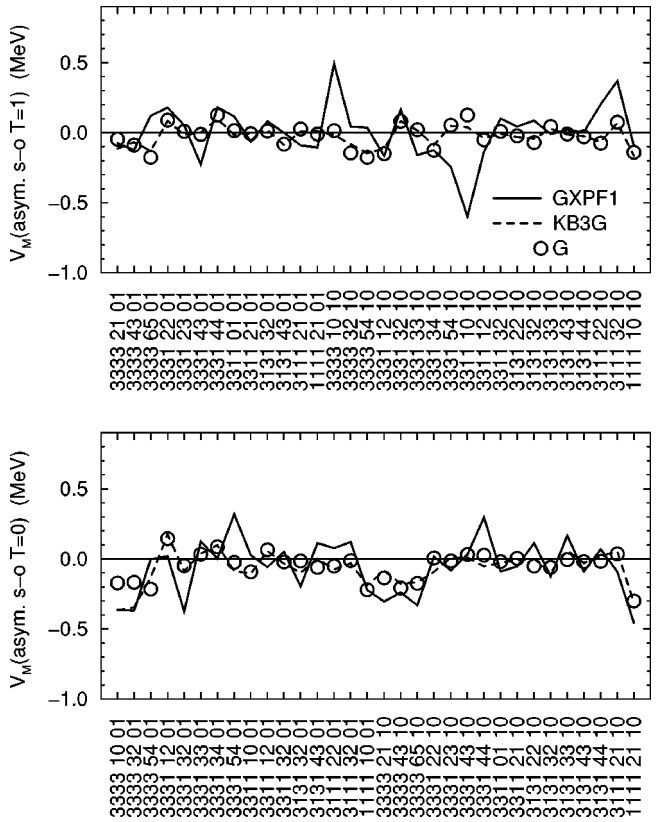

FIG. 7. Comparison of the antisymmetric spin-orbit components. Conventions are the same as in Fig. 4.

tion is 226 keV within FDA* for 623 energy data. Although this number sounds quite successful, GXPFM fails to describe N or $Z=28$ semimagic nuclei. In fact, for these nuclei, the estimated rms deviation increases to 267 keV for yrast states (87 data) and to 324 keV for yrare states (44 data).

We first consider the multipole part of the Hamiltonian. The collective strengths of the *p-h* interactions of GXPFM are found to have reasonable values. For example, $e^{20}=-2.85$, $e^{40}=-1.44$, and $e^{11}=+2.59$ (MeV), which are quite similar to those of GXPF1 (see Table IV). As for the *p-p* channel, since the multipole part of GXPFM is different from G only for the $T=1$ components, the strengths E^{10} and E^{20} are the same as those of G. On the other hand, the monopole pairing strength is reduced to $E^{01}=-3.88$, which is much weaker than that of GXPF1 and will compensate the large $T=0$ pairing strength.

Figure 8 compares the monopole matrix elements $V(ab;T)$ for GXPF1 and GXPFM. The $f_{7/2}$-related matrix elements of GXPFM take similar values to those of GXPF1 (and other interactions), although the $T=0$, f7f5 matrix element of GXPFM is more attractive than that of GXPF1 by 300 keV. Note that the monopole Hamiltonian is specified by the linear combinations $\frac{3}{4}V(ab;1)+\frac{1}{4}V(ab;0)$ and $V(ab;1)-V(ab;0)$, where the former determine, roughly speaking, the mass dependence and the latter affects the isospin dependence. The first combination is extremely well determined and almost identical between GXPF1 and GXPFM (differences are less than 50 keV).

Relatively large differences can be seen in the $T=1$, p3p3, f5f5, and p1p1 matrix elements, which are all related to the

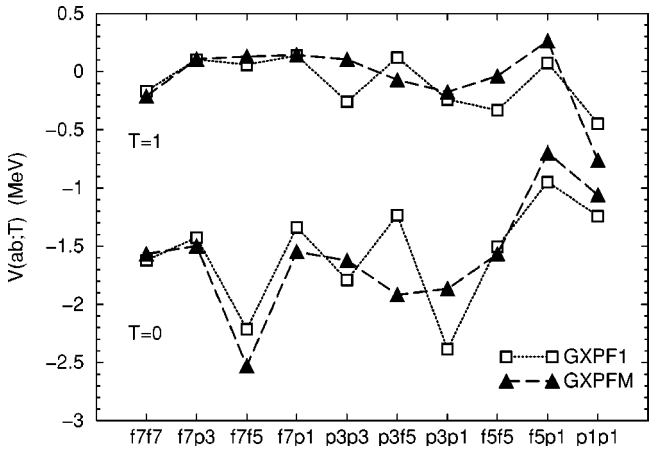

FIG. 8. Comparison of the monopole matrix elements $V(ab;T)$ for the GXPF1 and GXPFM interactions, which are shown by squares and triangles, respectively. Conventions are the same as in Fig. 2.

monopole pairing. The former two of GXPFM are less attractive than those of GXPF1, which is required to keep the collective monopole pairing strength weaker than that of GXPF1, as mentioned above. For the $T=0$ matrix elements, the p3f5 and p3p1 components are very different between GXPF1 and GXPFM. Although the structure of Ga and Ge isotopes is rather sensitive to these matrix elements, most of those isotopes cannot be included into the fit because N is too close to 40. This point may be clarified better in a future study including higher orbits.

III. RESULTS AND DISCUSSIONS

In this section, the results obtained from large-scale shell-model calculations with GXPF1 are given and compared with available experimental data. In our previous studies of *pf*-shell nuclei [1,10,28,29], we took advantage of the MCSM, which was the only feasible way to evaluate the eigenvalues of the shell-model Hamiltonian in the middle of the *pf* shell. In the present study, most of shell-model calculations are carried out in a conventional way by using the shell-model code MSHELL [30]. MSHELL enables calculations with M-scheme dimensions of up to $\sim 10^8$. With this capability we can handle essentially all low-lying states in the *pf*-shell nuclei with a minimal truncation of the model space. We can also confirm the reliability of the previous MCSM calculations by comparing both results. On the other hand, for nonyrast states in the middle of the *pf* shell, the MCSM is still necessary.

In the following discussions, the truncation order t denotes the maximum number of nucleons which are allowed to be excited from the $f_{7/2}$ orbit to higher three orbits $p_{3/2}$, $f_{5/2}$, and $p_{1/2}$, relative to the lowest filling configuration. The latter three orbits are expressed simply as r hereafter. Most results for Ca, Sc, Ti, V, Cr are exact (no truncation) while $t \geq 6$ for Mn, and $t \geq 5$ or better for other isotopes.

In this paper we fully cover the data on magnetic and quadrupole moments. Electromagnetic transitions are discussed for some representative nuclei. Gamow-Teller β de-

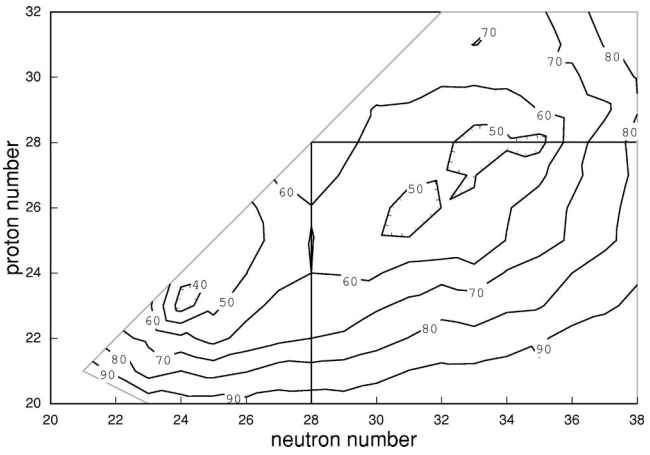

FIG. 9. The probability of ^{56}Ni closed-shell configurations in the calculated ground-state wave functions.

cay will be covered in subsequent work. Electromagnetic transition matrix elements are calculated by using the effective g factors and the effective charges adopted in Sec. III C and III D, respectively.

A. Closed core properties

First we consider the role of the Z or $N=28$ closed shell. This is important for the unified shell-model description of *pf*-shell nuclei, since it is convenient to base a truncation scheme on the stability of such a closed core. It has been shown [1] that the ^{56}Ni core is rather soft in comparison to the ^{48}Ca core. More precisely, the probability of the $(f_{7/2})^{16}$ configuration in the ground-state wave function of ^{56}Ni is much smaller than that of the $(f_{7/2})^{8}$ configuration in ^{48}Ca. It is attributed to the strong proton-neutron interaction. The evolution of such a closed core in various isotope chains is of interest.

Hereafter, a group of configurations in which both proton and neutron $f_{7/2}$ orbits are maximally filled will be denoted by the ^{56}Ni closed-shell configuration. For each isotope with Z_v valence protons and N_v valence neutrons on top of the ^{40}Ca core, such configurations are those given by $\pi(f_{7/2})^m(r)^{Z_v-m}\nu(f_{7/2})^n(r)^{N_v-n}$ with $m=\min\{Z_v,8\}$ and $n=\min\{N_v,8\}$. Figure 9 shows the probability of the closed-shell configurations in the calculated ground-state wave function. The lowest $T=0$ states are considered for odd-odd $N=Z$ isotopes, although they are not necessarily the ground states. The truncation order is taken to be sufficiently large for describing these states.

The probability takes the minimum value ($\sim$40%) around ^{48}Cr, which can be understood as a result of the large deformation. In the Ti isotopes, the probability becomes smallest around $N=24$ and then increases monotonously for larger N. On the other hand, in the case of Fe and Ni, one can see a local maximum ($\sim$60%) at $N=28$ and the second minimum ($\sim$45%) around $N=32-34$. Thus it is not justified to assume an inert ^{56}Ni core even for Ni isotopes. As for Zn isotopes, the probability shows rather smooth behavior with moderate values $\sim$65%, suggesting that the effects of core excitations are similar over the wide range of N.

B. Binding energy

Binding energies are obtained by adding suitable Coulomb energies to the shell-model total energies. In the present study the Coulomb energies are evaluated by using an empirical formula

$$E_{\mathrm{C}} = V_{\pi\pi}\frac{\pi(\pi-1)}{2} - V_{\pi\nu}\pi\nu + e_{\pi}\pi, \tag{6}$$

where π and ν denote the number of valence protons and neutrons, respectively. The adopted parameters are $V_{\pi\pi}=0.264$, $V_{\pi\nu}=0.038$, and $e_{\pi}=7.458$ (MeV). The same form was adopted in Ref. [31] for describing light *pf*-shell nuclei with a different parameter set. In the present approach, since we consider a wider mass region, the parameters are determined by fitting to the energy difference between 36 pairs of isobaric analog states with masses $A=47-74$. In Ref. [32], the binding energies are also studied systematically by using the KB3 interaction for many $f_{7/2}$ shell nuclei up to ^{56}Ni, and quite similar values of these parameters are proposed. They have attained an rms deviation of 215 keV between theory and experiment for 70 nuclei of $A=42-56$. However, the discrepancy in ^{56}Ni (overbinding) is significantly large in comparison to that of neighboring nuclei.

In Fig. 10 the deviation of calculated binding energies from experimental values are shown for each isotope chain as a function of the neutron number N. The theoretical values are obtained by GXPF1. For the truncations, all results are exact for Ca, Sc, Ti, V, and Cr isotopes. For other isotopes, the results are obtained in a subspace of $t=5$ or larger. Judging from the convergence pattern as a function of t, the underbinding due to this truncation is typically smaller than 200 keV. Note that the mass range included in the figure is much wider than that used in the fitting calculations for deriving GXPF1, and covers regions of nuclei which may not be well described just by the *pf* shell. It can be seen that the agreement between theory and experiment is quite good over the whole mass range included in the fit ($A=47-65$) and is also reasonable for many nuclei which were not included in the fit.

In the neutron-rich side, we can find relatively large deviations. In Ca and Sc isotopes, the calculations give overbinding at the end of the isotope chain, $N=32$ and 34, respectively, with large error bars in the experimental data. Note that, for ^{52}Ca, the experimental data was taken from Ref. [33], where the value $Q_{\beta^-}=7.9(5)$ MeV is adopted. On the other hand, in Ref. [34], the measured value $Q_{\beta^-}=5.7(2)$ MeV is presented. The prediction by GXPF1 is 5.9 MeV, in good agreement with the latter value. It is important to have improved experimental data for this neutron-rich region of nuclei. For the Ti isotopes, the agreement is satisfactory along the whole isotope chain. In other isotopes, the deviation between theory and experiment becomes sizable around $N\sim35$, and, for larger N, the calculation shows a systematic underbinding. For a fixed N, the deviation is largest for Cr, and it is moderate for V, Mn, Fe, Ge, and it is small for Co, Ni, Cu, Zn, Ga. We relate this to an increasing

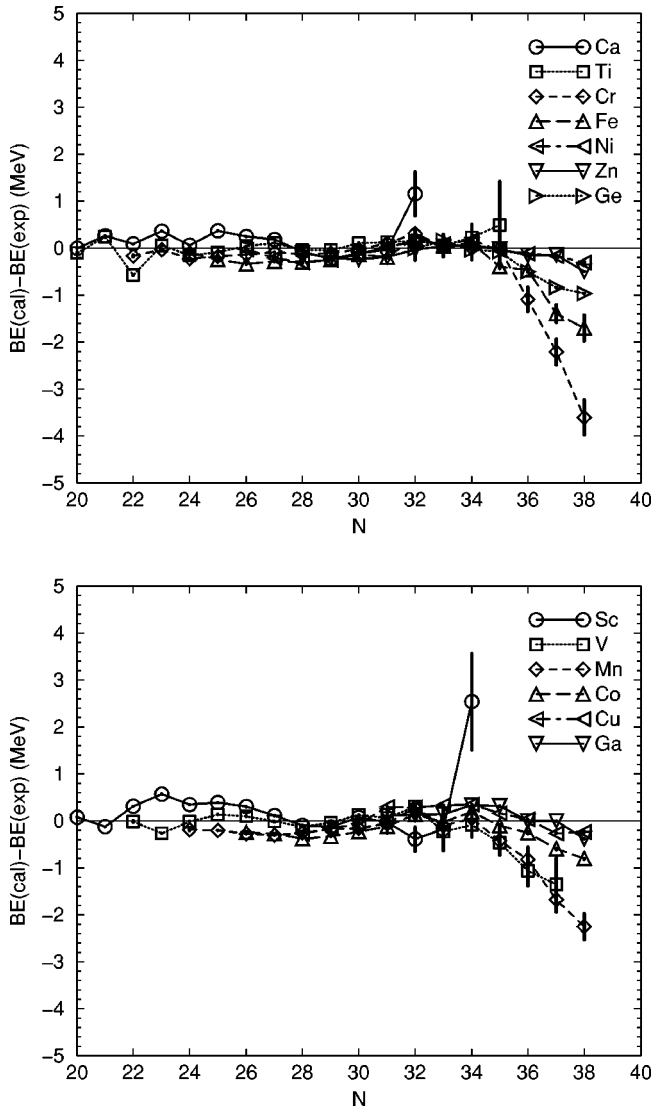

FIG. 10. Comparison of experimental binding energies with the shell-model energies. The upper (lower) panel shows the results of even- (odd-) Z isotope chains. Data are taken from Ref. [33].

importance of the neutron $g_{9/2}$ orbit which should have its maximal effect in the middle of proton $f_{7/2}$ shell (Cr) due to deformation.

C. Magnetic dipole moments

The magnetic dipole moments are calculated and compared with experimental data in Table V. The magnetic moment operator used in the present calculation is

$$\boldsymbol{\mu} = g_s \boldsymbol{s} + g_l \boldsymbol{l}, \tag{7}$$

where g_s and g_l are the spin and the orbital g factors, respectively. By using the free g factors g_s=5.586, g_l=1 for protons and g_s=−3.826, g_l=0 for neutrons, the agreement between the calculation ($\mu_{\rm theor}^{\rm free}$) and the experiment ($\mu_{\rm expt}$) is in general quite good.

Figure 11 shows the comparison of magnetic dipole moments between the experimental data and the shell-model predictions. The agreement appears to be good except for several cases to be discussed. As in the case of the *sd* shell [9], the description is successful already by using the free-nucleon g factors. It is well known that experimental magnetic moments deviate strongly from the single-particle (Schmidt) values, as seen, for example, on the left-hand side Fig. 37 of Ref. [35]. For the *sd* and *pf* shells we find that the configuration mixing within the shells is enough to fully account for observed magnetic moments. This is in contrast to Gamow-Teller β decay where the matrix elements of the isovector spin factor g_s are systematically reduced by factors of 0.77 in the *sd* shell [9] and 0.74 for the *pf* shell [36]. Thus, the good agreement obtained for the magnetic moments with the free-nucleon operator is interpreted as cancellation of the quenching observed in Gamow-Teller decay with enhancements in the spin and orbital electromagnetic operators due to exchange currents [9].

However, for the Ni and Zn isotopes, calculated values are systematically larger than the experimental ones by typically $0.2\mu_N$–$0.3\mu_N$. Such difficulties can be remedied to a certain extent by introducing the effective g factors, as shown in the same table ($\mu_{\rm theor}^{\rm eff}$). In the present calculation, we took $g_s^{\rm eff}=0.9g_s^{\rm free}$, g_l=1.1 and −0.1 for protons and neutrons, respectively, which were chosen from an estimate by the least-squares fit. It can be seen that the description of odd-A nuclei is systematically improved.

Nevertheless, deviations on order of $0.3\mu_N$ remain for the 2^+ state of Zn nuclei. We have examined the effect of a more general effective $M1$ operator which contains the $[Y_2 \boldsymbol{s}]^{(1)}$ term, but it turns out that the deviations for the Zn nuclei could not be remedied. It may be required to include the $g_{9/2}$ orbit to improve the description of these states, as also discussed in Ref. [43]. One may also want to reexamine the systematic uncertainties which may exist in the effective transient fields which are used to deduce magnetic moments from the experimental data.

There are a few other cases where we find large differences between theory and experiment. Several of these can be interpreted as a consequence of incorrect mixing of two closely lying states. For example, in ^{55}Fe, the first and the second $7/2^-$ states are separated only by 92 keV experimentally. The GXPF1 predicts these states in the reversed order. It is also the case for two $3/2^-$ states of ^{65}Zn, where the experimental energy separation is 92 keV.

We also find notable differences between theory and experiment for ^{50}Cr 8^+, ^{54}Mn 5^+, ^{58}Co 3^+, ^{47}Ti $7/2^-$, and ^{51}Cr $3/2^-$ where experimental uncertainties are also large. More precise measurements of these are required. The deviations in ^{65}Cu $5/2^-$ and ^{66}Cu 1^+ may be attributed to the effect of $g_{9/2}$ orbit. The deviations in ^{70}Zn and ^{72}Ge are naturally understood as a result of the insufficient model space.

D. Electric quadrupole moments

The electric quadrupole moments are given in Table VI. The effective charges e_π=1.5, e_ν=0.5 are adopted in the present calculations. The correlation between the calculated electric quadrupole moments and the experimental data is shown in Fig. 12. One can find that, in general, the deviation

TABLE V. Comparison of experimental magnetic dipole moments μ_{expt} (in unit of μ_N) with theoretical values $\mu_{\mathrm{theor}}^{\mathrm{free}}$ and $\mu_{\mathrm{theor}}^{\mathrm{eff}}$, which are calculated by using the free and the effective g factors, respectively. Most of the data are taken from Ref. [37]. All results for Ca, Sc, Ti, V, and Cr are exact, while $t \geqslant 6$ for Mn and $t \geqslant 5$ for other isotopes.

Nuclei	State	E_x (MeV)	μ_{expt}	$\mu_{\mathrm{theor}}^{\mathrm{free}}$	$\mu_{\mathrm{theor}}^{\mathrm{eff}}$
^{47}Ca	$7/2^-$	0.000	−1.380(24)	−1.464	−1.629
^{49}Ca	$3/2^-$	0.000	−1.38(6)	−1.403	−1.376
^{47}Sc	$7/2^-$	0.000	+5.34(2)	5.054	5.063
^{47}Ti	$5/2^-$	0.000	−0.78848(1)	−0.741	−0.844
	$7/2^-$	0.159	−1.9(6)	−0.824	−0.968
^{48}Ti	2^+	0.984	+0.784(38)[a]	0.650	0.574
	4^+	2.296	+2.16(52)[a]	1.949	1.863
^{49}Ti	$7/2^-$	0.000	−1.10417(1)	−1.083	−1.247
^{50}Ti	2^+	1.554	2.89(15)[b]	2.473	2.455
	6^+	3.199	+9.3(10)	8.170	8.306
^{48}V	4^+	0.000	2.012(11)	2.023	1.934
	2^+	0.308	0.444(16)	0.424	0.410
^{49}V	$7/2^-$	0.000	4.47(5)	4.335	4.383
	$3/2^-$	0.153	+2.37(12)	2.259	2.286
^{50}V	6^+	0.000	+3.3456889(14)	3.202	3.097
^{51}V	$7/2^-$	0.000	+5.14870573(18)	4.849	4.931
	$5/2^-$	0.320	+3.86(33)	3.165	3.271
^{49}Cr	$5/2^-$	0.000	0.476(3)	−0.493	−0.571
	$(19/2^-)$	4.365	+7.4(12)	6.427	6.354
^{50}Cr	2^+	0.783	+1.238(52)[a]	1.125	1.103
	4^+	1.881	+3.1(5)[a]	2.957	2.976
	6^+	3.164	+3.2(10)	4.044	4.027
	8^+	4.745	+4.3(7)	6.333	6.345
^{51}Cr	$7/2^-$	0.000	(−)0.934(5)	−0.829	−0.989
	$3/2^-$	0.749	−0.86(12)	−0.317	−0.288
^{52}Cr	2^+	1.434	+2.41(13)[a]	2.220	2.272
^{53}Cr	$3/2^-$	0.000	−0.47454(3)	−0.607	−0.587
	$7/2^-$	1.290	+2.8(49)	1.199	1.233
^{54}Cr	2^+	0.835	1.68(11)[c]	1.281	1.279
^{51}Mn	$5/2^-$	0.000	3.5683(13)	3.476	3.503
^{52}Mn	6^+	0.000	+3.063(1)	3.149	3.041
	2^+	0.378	+0.00768(8)	−0.005	−0.069
^{53}Mn	$7/2^-$	0.000	5.024(7)	4.746	4.843
	$5/2^-$	0.378	+3.25(30)	3.402	3.467
^{54}Mn	3^+	0.000	+3.2819(13)	3.234	3.311
	2^+	0.055	3.4^{+28}_{-16}	3.762	3.797
	4^+	0.156	+5.1(10)	3.538	3.650
	5^+	0.368	+38(21)	4.078	4.188
	6^+	1.073	2.8(15)	2.965	2.818
^{55}Mn	$5/2^-$	0.000	3.4532(13)	3.387	3.429
	$7/2^-$	0.126	4.4(7)	4.408	4.480
^{56}Mn	3^+	0.000	+3.2266(2)	3.494	3.420
^{53}Fe	$3/2^-$	0.741	−0.386(15)	−0.464	−0.444
^{54}Fe	2^+	1.408	+2.10(12)[b]	2.087	2.187
	6^+	2.949	8.22(18)	7.848	8.023
	10^+	6.527	+7.281(10)	7.176	7.110

TABLE V. (*Continued.*)

Nuclei	State	E_x (MeV)	$\mu_{\rm expt}$	$\mu^{\rm free}_{\rm theor}$	$\mu^{\rm eff}_{\rm theor}$
^{55}Fe	$5/2^-$	0.931	+2.7(12)	1.314	1.133
	$7/2^-$	1.317	+2(2)	−0.553	−0.717
	$7/2^-$	1.409	−2.2(5)	1.493	1.596
^{56}Fe	2^+	0.847	+1.22(16)	1.176	1.183
^{57}Fe	$1/2^-$	0.000	+0.09044(7)	0.241	0.162
	$3/2^-$	0.014	−0.1549(2)	−0.266	−0.312
	$5/2^-$	0.137	+0.935(10)	1.052	0.833
^{58}Fe	2^+	0.811	+0.92(26)	1.206	1.209
^{59}Fe	$3/2^-$	0.000	−0.3358(4)[d]	−0.203	−0.251
^{55}Co	$7/2^-$	0.000	+4.822(3)	4.630	4.746
^{56}Co	4^+	0.000	3.851(12)	3.652	3.774
^{57}Co	$7/2^-$	0.000	+4.720(10)	4.616	4.704
	$3/2^-$	1.378	+3.0(6)	2.220	2.140
^{58}Co	2^+	0.000	+4.044(8)	4.229	4.332
	4^+	0.053	+4.194(8)	4.218	4.166
	3^+	0.112	+2.2(4)	3.954	3.969
^{59}Co	$7/2^-$	0.000	+4.627(9)	4.637	4.707
	$3/2^-$	1.292	+2.54(12)	2.794	2.868
^{60}Co	5^+	0.000	+3.799(8)	3.962	3.996
	2^+	0.059	+4.40(9)	4.349	4.378
^{57}Ni	$3/2^-$	0.000	−0.7975(14)[d]	−0.789	−0.802
^{58}Ni	2^+	1.454	+0.076(17)[e]	−0.017	−0.096
^{59}Ni	$5/2^-$	0.339	+0.35(15)	0.744	0.482
^{60}Ni	2^+	1.333	+0.32(6)[e]	0.496	0.412
^{61}Ni	$3/2^-$	0.000	−0.75002(4)	−0.688	−0.707
	$5/2^-$	0.067	+0.480(6)	0.787	0.516
^{62}Ni	2^+	1.173	+0.33(6)[e]	0.780	0.686
^{63}Ni	$5/2^-$	0.087	+0.752(3)	1.042	0.730
^{64}Ni	2^+	1.346	+0.37(6)[e]	0.510	0.375
^{65}Ni	$5/2^-$	0.000	0.69(6)	1.101	0.767
^{67}Ni	$(1/2^-)$	0.000	0.601(5)	0.547	0.425
^{60}Cu	2^+	0.000	+1.219(3)	1.258	1.159
^{61}Cu	$3/2^-$	0.000	+2.14(4)	2.258	2.193
^{62}Cu	1^+	0.000	−0.380(4)	−0.157	−0.236
	2^+	0.041	+1.32(3)	1.350	1.210
	4^+	0.390	+2.67(16)	2.941	2.663
^{63}Cu	$3/2^-$	0.000	+2.22329(18)	2.314	2.251
^{64}Cu	1^+	0.000	−0.271(2)	−0.023	−0.114
^{65}Cu	$3/2^-$	0.000	+2.3817(3)	2.496	2.398
	$5/2^-$	1.115	+4.5(9)	1.592	1.515
^{66}Cu	1^+	0.000	−0.282(2)	0.616	0.490
^{62}Zn	2^+	0.954	+0.74(20)[f]	1.176	1.161
^{63}Zn	$3/2^-$	0.000	−0.28164(5)	−0.243	−0.282
^{64}Zn	2^+	0.992	+0.89(9)[f]	1.239	1.200
^{65}Zn	$5/2^-$	0.000	+0.7690(2)	1.027	0.753
	$3/2^-$	0.115	−0.78(20)	0.511	0.393
	$3/2^-$	0.207	+0.73(25)	−0.583	−0.579
^{66}Zn	2^+	1.039	+0.80(8)[f]	1.238	1.171

TABLE V. (*Continued.*)

Nuclei	State	E_x (MeV)	μ_{expt}	$\mu_{\text{theor}}^{\text{free}}$	$\mu_{\text{theor}}^{\text{eff}}$
^{67}Zn	$5/2^-$	0.000	+0.87548(1)	1.229	0.914
	$1/2^-$	0.093	+0.587(11)	0.595	0.492
	$3/2^-$	0.185	+0.50(6)	0.679	0.543
^{68}Zn	2^+	1.077	+0.87(9)[f]	1.489	1.363
^{70}Zn	2^+	0.885	+0.76(8)[f]	3.757	3.704
^{66}Ga	$(2)^+$	0.066	1.011(18)	1.056	0.874
	(9^+)	3.043	4.2(9)	4.443	4.422
^{67}Ga	$3/2^-$	0.000	+1.8507(3)	1.792	1.786
	$5/2^-$	0.359	1.40(65)	1.310	1.584
^{68}Ga	1^+	0.000	0.01175(6)	0.188	0.003
^{69}Ga	$3/2^-$	0.000	+2.01659(4)	1.850	1.840
^{71}Ga	$3/2^-$	0.000	+2.56227(2)	2.782	2.748
^{69}Ge	$5/2^-$	0.000	0.735(7)	1.063	0.757
^{70}Ge	2^+	1.039	+0.936(52)	0.789	0.671
^{71}Ge	$1/2^-$	0.000	+0.547(5)	0.346	0.250
	$5/2^-$	0.175	+1.018(10)	1.255	0.909
^{72}Ge	2^+	0.834	+0.798(66)	2.314	2.469

[a]Data from Ref. [38].
[b]Data from Ref. [39].
[c]Data from Ref. [40].
[d]Data from Ref. [41].
[e]Data from Ref. [42].
[f]Data from Ref. [43].

of the theoretical prediction from the experimental data becomes large where the experimental error bar is also large, except for a few cases. The sign of the calculated $Q(3/2^-)$ for ^{57}Co is opposite to the experimental data. This result suggests an incorrect mixing of the first and the second $3/2^-$ states in the calculation, which are close in energy (380 keV experimentally). The calculated $3/2_2^-$ state lies 589 keV above $3/2_1^-$ state with $Q=+0.138\ e$b, which is consistent with this interpretation. The description of ^{64}Zn 2^+ is also very poor, but the uncertainty in the data is large. The description is unsuccessful for ^{70}Zn, ^{70}Ge, and ^{72}Ge, indicating the need for introducing the $g_{9/2}$ orbit.

E. Systematics of 2_1^+ states

The first 2^+ state of an even-even nucleus is a good systematic measure of the structure. The left panel of Fig. 13 shows the excitation energies of the 2_1^+ states for Ca, Ti, Cr, Fe, Ni, Zn, and Ge isotopes. The results except for Zn and Ge isotopes have already been discussed in our previous paper [7]. The lightest nucleus in each isotope chain is taken to be $N=Z$ (cases with $N<Z$ have mirror nuclei similar properties). The overall description of the 2^+ energy levels is reasonable for all these isotope chains, although the calculated energies are systematically higher than experimental ones by about 200 keV. In all cases, the energy jump corre-

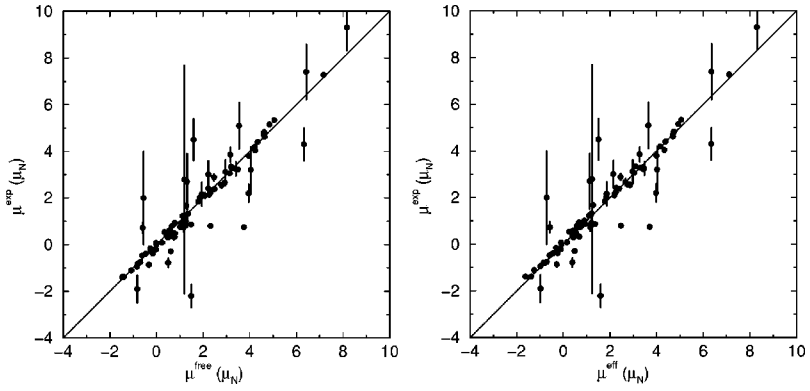

FIG. 11. Comparison of experimental magnetic dipole moments with the shell-model results, which were obtained by using the free (left panel) and effective (right panel) nucleon g factors. All data in Table V are included for which the sign is measured experimentally.

TABLE VI. Comparison of experimental electric quadrupole moments Q_{expt} (in unit of e fm^2) with theoretical values Q_{theor}, which are calculated by using the effective charges $e_\pi=1.5$, $e_\nu=0.5$. Data are taken from Ref. [37].

Nuclei	State	E_x (MeV)	Q_{expt}	Q_{theor}
^{47}Ca	$7/2^-$	0.000	+2.1(4)	6.7
^{47}Sc	$7/2^-$	0.000	−22(3)	−20.6
^{47}Ti	$5/2^-$	0.000	+30.3(24)	21.6
^{48}Ti	2^+	0.984	−17.7(8)	−12.6
^{49}Ti	$7/2^-$	0.000	+24(1)	22.0
^{50}Ti	2^+	1.554	+8(16)	6.2
^{50}V	6^+	0.000	+20.9(40)	19.0
^{51}V	$7/2^-$	0.000	−4.3(5)	−6.3
^{50}Cr	2^+	0.783	−36(7)	−26.4
^{52}Cr	2^+	1.434	−8.2(16)	−12.3
^{53}Cr	$3/2^-$	0.000	−15(5)	−15.3
^{54}Cr	2^+	0.835	−21(8)	−24.4
^{51}Mn	$5/2^-$	0.000	42(7)	34.8
^{52}Mn	6^+	0.000	+50(7)	50.5
^{54}Mn	3^+	0.000	+33(3)	33.2
^{55}Mn	$5/2^-$	0.000	+33(1)	35.4
^{54}Fe	2^+	1.408	−5(14)	−22.6
	10^+	6.527	58(6)[a]	53.5
^{56}Fe	2^+	0.847	−19(8)	−27.4
^{57}Fe	$3/2^-$	0.014	16(1)[b]	15.8
^{58}Fe	2^+	0.811	−27(5)	−27.9
^{56}Co	4^+	0.000	+25(9)	28.2
^{57}Co	$7/2^-$	0.000	+52(9)	36.0
	$3/2^-$	1.378	+22(3)	−22.5
	$3/2^-$	1.758		13.8
^{58}Co	2^+	0.000	+22(3)	22.3
^{59}Co	$7/2^-$	0.000	+40(4)	40.4
^{60}Co	5^+	0.000	+44(5)	50.7
	2^+	0.059	+30(40)	26.3
^{58}Ni	2^+	1.454	−10(6)	−2.4
^{60}Ni	2^+	1.333	+3(5)	3.9
^{61}Ni	$3/2^-$	0.000	+16.2(15)	14.2
	$5/2^-$	0.067	−20(3)	−19.5
^{62}Ni	2^+	1.173	+5(12)	25.3
^{64}Ni	2^+	1.346	+35(20)	10.9
^{63}Cu	$3/2^-$	0.000	−21.1(4)	−20.4
^{65}Cu	$3/2^-$	0.000	−19.5(4)	−19.0
^{63}Zn	$3/2^-$	0.000	+29(3)	20.8
^{64}Zn	2^+	0.992	−32(6) or −26(6)	−7.4
^{65}Zn	$5/2^-$	0.000	−2.3(2)	−4.8
^{67}Zn	$5/2^-$	0.000	15.0(15)	16.1
^{70}Zn	2^+	0.885	−23.3(22)	−2.5
^{67}Ga	$3/2^-$	0.000	19.5	19.6
^{68}Ga	1^+	0.000	2.77(14)	−1.3
^{69}Ga	$3/2^-$	0.000	+16.8	17.5
^{71}Ga	$3/2^-$	0.000	+10.6	12.8
^{69}Ge	$5/2^-$	0.000	2.4(5)	6.8

TABLE VI. (*Continued.*)

Nuclei	State	E_x (MeV)	Q_{expt}	Q_{theor}
^{70}Ge	2^+	1.039	+3(6)	19.8
^{72}Ge	2^+	0.834	−13(6)	13.2

[a]Data evaluated based on the data b combined with a constraint $Q(^{54}\text{Fe};10^+)/Q(^{57}\text{Fe};3/2^-)=3.62\pm0.22$ [45] from a Mössbauer analysis.
[b]Data from Ref. [44].

sponding to $N=28$ shell closure is nicely reproduced for Ca to Ni isotopes. In the case of Zn isotopes, $E_x(2_1^+)$ is almost constant, which is also well reproduced. Recently measured value for ^{54}Ti ($N=32$) [46] comes precisely on the prediction of GXPF1. The new data of ^{58}Cr ($N=34$) [47] also follows the predicted systematics.

Very recent data for ^{56}Ti gives a 2^+ energy of 1.13 MeV [48]. This is significantly lower than the GPFX1 prediction of 1.52 MeV. The KB3G interaction gives 0.89 MeV for the ^{56}Ti 2^+, and experiment lies in between GPFX1 and KB3G. The dominant neutron component of this 2^+ state has one neutron in the $f_{5/2}$ orbit. In ^{54}Ti there are some high spin states whose wave functions are dominated by the configuration with one neutron in the $f_{5/2}$ orbit, and their experimental energies are about 400 keV lower than GXPF1 and in between GPFX1 and KB3G [46]. The implication is that the effective single-particle energy for the neutron $f_{5/2}$ orbit in $Z=22$ is about 800 keV too high compared with GPFX1. The strong monopole interaction between the proton $f_{7/2}$ orbit and the neutron $f_{5/2}$ orbit [18] is responsible for lowering the energy of the $f_{5/2}$ neutron energy (relative to $p_{3/2}$) as protons are added to the $f_{7/2}$ orbit from $Z=20$ to 28 (see the right-hand side of Fig. 1 in Ref. [7]). Thus to improve the agreement for ^{56}Ti, one would need to reduce the strength of these two-body matrix elements in a way which is consistent with the entire fit. This will be one of the considerations for a next generation interaction. The $N=34$ gap between $p_{1/2}$ and $f_{5/2}$ is about 4 MeV. If it is estimated too large by 800 keV by the GXPF1 interaction, the real gap turns out be greater than 3 MeV. Thus, this very new data seem to support the appearance of $N=34$ gap, while details of the GXPF1 interaction may have to be improved. One must be also aware of the small separation energy of $f_{5/2}$ in some of the nuclei being discussed here. Such a small separation energy induces ad-

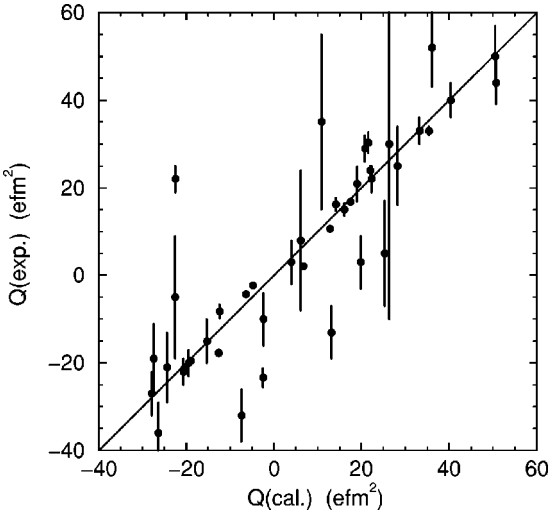

FIG. 12. Comparison of experimental electric quadrupole moments with the shell-model results. All data in Table VI are included for which the sign is measured experimentally.

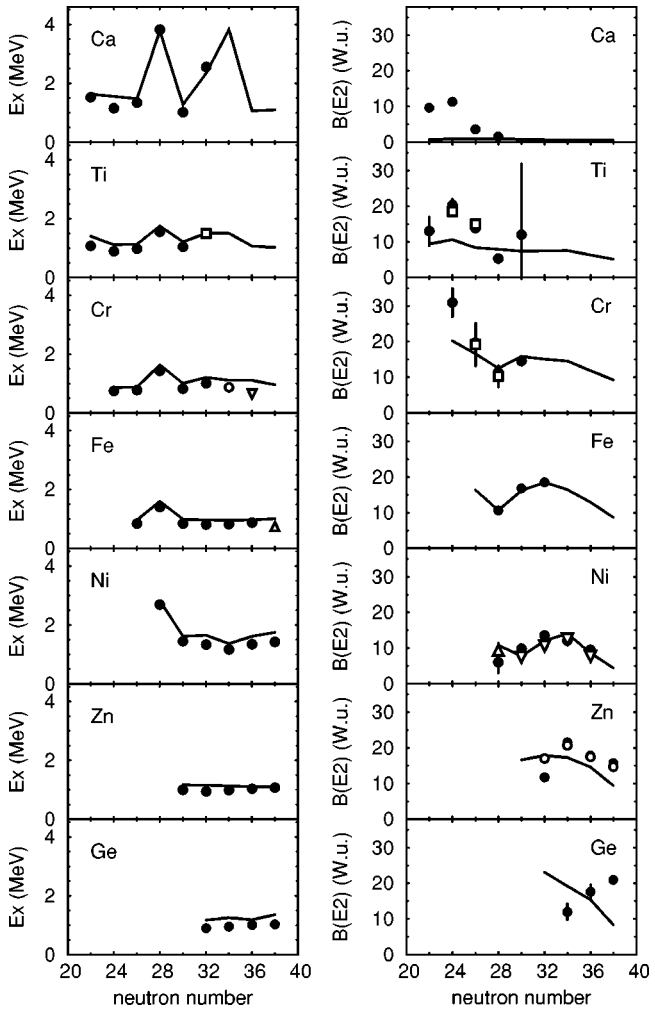

FIG. 13. (Left) First 2^+ energy levels as a function of the neutron number N. Experimental data are shown by filled circles [37], squares [46], open circles [47], triangles (down) [49], and triangles (up) [51]. Solid lines show results of shell-model calculations. The truncation order t is 5 for ^{56,58}Fe, ^{60}Ni, ^{60,62,64}Zn, 6 for ^{56,58,62}Ni, and 7 for ^{52,54}Fe. The other results are exact. (Right) The values of $B(E2;2_1^+\rightarrow 0_1^+)$. Experimental data are shown by filled circles [37], squares [39], triangles (up) [52], triangles (down) [42], and open circles [43].

ditional relative lowering of $f_{5/2}$, whereas this effect becomes weaker in nuclei with more protons. This effect is not included in the present fit, because it is not sizable in the nuclei used for the fit.

The 2^+ level for ^{60}Cr($N=36$) [49] deviates toward lower energy as compared to the GXPF1 prediction. This is correlated with the deviation in binding energy, and both are signatures of more collectivity from mixing with $g_{9/2}$. In the Fe isotopes, a similar deviation can be seen at $N=38$. These results suggest the limitation of the reliability of GXPF1 interaction for neutron-rich nuclei. It is likely that one will need to explicitly introduce the $g_{9/2}$ orbit into the model space in order to improve the calculations as one approaches $N=40$.

In the right panel of Fig. 13, the $E2$ transition matrix elements $B(E2;2_1^+ \rightarrow 0_1^+)$ are shown. Experimental $B(E2)$ are significantly larger than theory for $N \leqslant 24$, especially for the Ca isotopes, although the agreement in the excitation energy of 2_1^+ state is reasonable. These deviations show the large effects of the core excitation that has long been known for nuclei such as ^{42}Ca [50]. The ^{40}Ca core is significantly broken and we should take into account the excitation from the *sd* shell explicitly in order to reproduce these $B(E2)$ values. On the other hand, the agreement between theory and experiment is quite good in the middle of the shell, especially for Fe and Ni isotopes. The dependence on the neutron number is nicely reproduced including the $N=28$ magic number. For Zn and Ge isotopes with $N \geqslant 34$, we again see the need of more collectivity in the model space, which also suggests the necessity of the $g_{9/2}$ orbit, consistently with the results of electromagnetic moments discussed in the previous sections.

F. Semimagic nuclei

In this section, spectroscopic properties are studied in detail for several N or $Z=28$ nuclei around ^{56}Ni. If we assume an inert closed core for ^{56}Ni, these semimagic nuclei are described by a few valence nucleons of one kind, i.e., only proton holes or only neutron particles. Therefore, the low-lying level density is rather low and the effects of core excitations are easy to interpret. In fact, it has been pointed out in Ref. [53] that, although the shell-model calculation in a truncated $t \leqslant 2$ subspace is quite successful for describing most of the low-lying states in $N=28-30$ nuclei, it is impossible to reproduce those states which contain sizable broken-core components, such as the lowest excited states in ^{55}Co, excited states above the lowest $3/2^-, 5/2^-, 1/2^-$ triplets in ^{57}Ni, excited 0^+ in ^{54}Fe and ^{58}Ni, etc. Similar difficulties can be seen also in Ref. [54], where the shell-model calculations in a truncated space have been carried out with a different effective interaction. Note that the cause of this problem lies not only in the truncation of the model space but also in the effective interaction itself. It is well known that the KB3 interaction (and also its descendants) gives an excellent description for low-lying states of $A \leqslant 52$ nuclei, but KB3 fails around ^{56}Ni, even when the model space is sufficiently large for convergence. Thus it is interesting to investigate whether GXPF1 can properly describe these low-lying states which are sensitive to the core exitation. We consider semimagic nuclei with $Z=25,26,27$ and $N=29,30,31$.

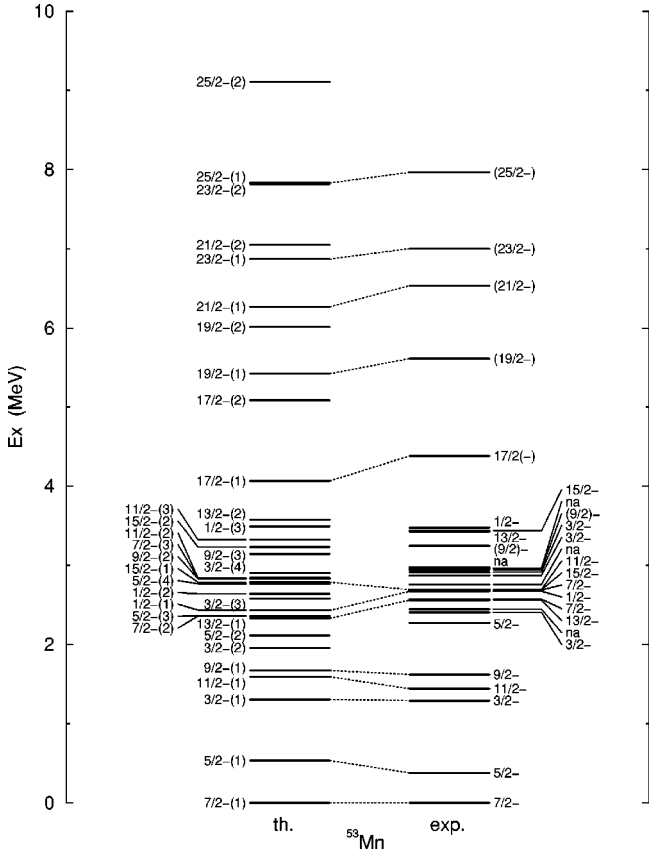

FIG. 14. Experimental (right) and calculated (left) energy levels of ^{53}Mn. Experimental data are taken from Ref. [55]. The label "na" indicates that the spin-parity is not assigned experimentally. The calculated yrast states are connected with experimental counterparts (or their candidates) by dotted lines.

1. ^{53}*Mn*

Figure 14 shows experimental and calculated energy levels of ^{53}Mn. Most of the theoretical energy levels are obtained in the $t=7$ subspace. The exact ($t=13$) results are also obtained in some cases. All experimental energy levels below 3 MeV excitation energy as well as the yrast states are shown with their theoretical counterparts and several additional states.

For the yrast states, the agreement between the theory and the experiment is quite good. Assuming an inert ^{56}Ni core, this nucleus is described by three neutron holes in the $f_{7/2}$ orbit. Under such an assumption, possible states are $J^\pi = 3/2^-, 5/2^-, 7/2^-, 9/2^-, 11/2^-$, and $15/3^-$. In the calculated wave functions, the lowest $(f_{7/2})^{13}$ configuration is in fact dominant (46–60%) for the yrast states of these spin-parities. Therefore, the truncation of the model space by a small $t \sim 2$ is reasonable for these states.

Other yrast states $1/2^-$, $13/2^-$, $17/2^-$, $19/2^-$, $21/2^-$, $23/2^-$, and $25/2^-$ consist mainly of $\pi(f_{7/2})^5 \nu(f_{7/2})^7 (p_{3/2})^1$ and $\pi(f_{7/2})^5 \nu(f_{7/2})^7 (f_{5/2})^1$ configurations. These states are also well reproduced in the calculation, indicating that the effective single-particle gap above $N=28$ is reasonably reproduced in the present interaction.

In order to investigate the properties of the core in detail, it is important to consider nonyrast states which contain a

large amount of multiparticle excitations from the $N=28$ core. Above $E_x \sim 2.2$ MeV, the experimental level density increases significantly, which is well reproduced in the calculation. The largest difference between the experiment and the calculation is found for the $3/2_2^-$ state which lies at lower energy by 450 keV in the calculation, resulting in the inversion of $5/2_2^-$ and $3/2_2^-$. Nevertheless, one can find reasonable one-to-one correspondence between the experimental and theoretical energy levels.

Focusing on the neutron configuration, the main configuration of these nonyrast states is $\nu(f_{7/2})^7(r)^1$ [r stands for $(p_{3/2}, f_{5/2}, p_{1/2})$]. The typical probability for the neutron 1p-1h configuration is ~60%. These states contain also multineutron excitations as 2p-2h (~25%) and 3p-3h (~7%). Therefore, taking into account the proton excitation, the $t \sim 4$ subspace is reasonable for describing these states.

However, even in this energy region of $E_x \sim 2.5$ MeV, there are several states in which the $N=28$ core is more severely broken. In $5/2_2^-$, $7/2_2^-$, $9/2_2^-$, the main neutron configuration is 2p-2h type (~60%), and also there are sizable broken-core components such as 3p-3h (~17%) and 4p-4h (~6%). Evidently, the $t=4$ subspace is no longer sufficient and at least $t=6$ is needed to describe these states properly. In fact, for example, the electric quadrupole moment for $5/2_2^-$ varies as $Q(5/2_2^-) = -0.25$, +0.32, +0.36, and +0.37 eb for $t=4,5,6$, and 13 (exact), respectively. The change of the sign in going from $t=4$ to $t=5$ is due to the crossing of $5/2_2^-$ and $5/2_3^-$. A similar crossing is found in the case of $7/2_2^-$. Although these neutron 2p-2h states are connected by relatively large (collective) $M1$ and $E2$ transition matrix elements as $B(E2; 7/2_2^- \to 5/2_2^-) = 34$ W.u. and $B(M1; 7/2_2^- \to 5/2_2^-) = 0.17$ W.u. (W.u. stands for Weisskopf unit), it may be difficult to observe such transitions because of negligibly small γ-ray energies in comparison to the transition to the yrast states.

In Table VII, calculated electromagnetic transition probabilities are compared with experimental data. Reasonable agreement can be seen in most cases, including transitions between nonyrast states. Note that the theoretical $1/2_2^-$ is assigned to the experimental $1/2^-$ at 2671 keV so that the transition data can be consistently described.

2. ^{54}Fe

In Fig. 15, the energy levels of ^{54}Fe are compared with experimental data. All experimental energy levels below $E_x = 4$ MeV and all yrast states are shown with their theoretical counterparts. Shell-model calculations have been carried out in the $t=7$ or larger subspace including the exact ($t=14$). One can see remarkable one-to-one correspondence between theory and experiment for most of these levels.

The yrast band 0^+-2^+-4^+-6^+ shows a typical proton–two hole spectrum in the $f_{7/2}$ orbit under the influence of a short range interaction. In fact the wave functions of these states are dominated by the $\pi(f_{7/2})^6\nu(f_{7/2})^8$ configuration (50–60%). On the other hand, the yrast 8^+ and 10^+ states consist of core-excited configurations. While the dominating configurations are still of neutron 1p-1h excitation type from the $N=28$ core (36% and 57% for 8^+ and 10^+ states, respectively), the wave functions can no longer be approximated by only one configuration. The energy gap between 6^+ and 8^+ reflects the softness of the ^{56}Ni core, which is determined by the effective interaction. It is shown in Ref. [56] that the energy gap is too large with the KB3 interaction. This is consistent with the fact that it also gives an energy for the yrast 2^+ energy in ^{56}Ni which is too high compared with experiment.

It was pointed out in Ref. [29] that the FPD6 [26] interaction predicts the existence of deformed states at relatively low excitation energy (~3 MeV), which consist of neutron 2p-2h configurations. In the present calculation, the candidates of such states appear as 0_2^+ and 2_3^+. The neutron 2p-2h configuration is 35% and 26% in these states, respectively, which are the most dominant components in their wave functions. However, the deformation of these states is much smaller than the FPD6 prediction. The electric quadrupole moment for the "2p-2h" 2^+ state is predicted to be -0.30 eb [29] by the variation after the angular momentum projection method with the FPD6 interaction. On the other hand, in the present results, it is $Q(2_3^+) = -0.09$ eb, and the $E2$ transition matrix element is $B(E2; 2_3^+ \to 0_2^+) = 11.3$ W.u., which is slightly larger than that of the yrast in-band transition. These values are inconsistent with the axially symmetric large prolate deformation. In the present results, two neutrons are excited mainly to the $p_{3/2}$ orbit, while it is $f_{5/2}$ in the results of the FPD6 interaction, reflecting the fact that the effective single-particle energy for the $f_{5/2}$ orbit is too low for FPD6.

In Table VIII, the calculated electromagnetic transition matrix elements are compared with experimental data. The $E2$ transition matrix elements in the ground-state band are reproduced fairly well in the present calculations, although the $8^+ \to 6^+$ transition is overestimated. Such a deviation is commonly seen also in the results of KB3 and FPD6 interactions [56]. Other $B(E2)$ values are reasonably reproduced except for several of the small ones. As for the $B(M1)$ values, the agreement between theory and experiment is basically good. The exception is $4^+(3294) \to 4^+(2538)$ transition, which is significantly overestimated by more than one order of magnitude in the present calculation.

3. ^{55}Co

In Fig. 16, energy levels of ^{55}Co are shown. All experimental energy levels below $E_x = 4$ MeV and all yrast states up to $J^\pi = 23/2^-$ are compared with theoretical results. There is a state with unknown spin-parity at $E_x = 2.960$ MeV, which can be interpreted tentatively as a $5/2^-$ state in correspondence to the present calculation. The overall agreement between theory and experiment is quite good.

If we assume an inert ^{56}Ni core, this nucleus is described as one neutron hole in the $f_{7/2}$ orbit, corresponding to only one $7/2^-$ state. In the calculated ground-state wave function, the probability of this 0p-1h configuration relative to the ^{56}Ni core is only 65%, and there are sizable (~20%) 2p-3h configurations. All excited states consist of core-broken configurations even in the lowest order of the approximation. Therefore the property of the core is expected to manifest clearly in the yrast spectrum.

TABLE VII. $B(M1)$ and $B(E2)$ for ^{53}Mn. The excitation energy E_x is shown in keV. Experimental data are taken from Ref. [55].

Initial $J^\pi(E_x)$	Final $J^\pi(E_x)$	Multipole	Expt. (W.u.)	Theor. (W.u.)
$5/2^-(378)$	$7/2^-(0)$	$M1$	0.00254(23)	0.0060
		$E2$	14(3)	21.7
$3/2^-(1290)$	$5/2^-(378)$	$M1$	0.023(3)	0.0194
		$E2$	1.9(5)	0.6
	$7/2^-(0)$	$E2$	13.4(11)	8.1
$11/2^-(1441)$	$7/2^-(0)$	$E2$	12.8(18)	9.4
$9/2^-(1620)$	$5/2^-(378)$	$E2$	3.7(6)	3.6
	$7/2^-(0)$	$M1$	0.0012(3)	0.0002
		$E2$	7.0(9)	5.4
$5/2^-(2274)$	$3/2^-(1290)$	$M1$	0.0021(8)	0.0000
		$E2$	3.0(15)	0.0
	$5/2^-(378)$	$M1$	0.0019(4)	0.0010
		$E2$	0.61(14)	1.6
	$7/2^-(0)$	$M1$	0.0054(11)	0.0023
		$E2$	0.07(4)	0.02
$3/2^-(2407)$	$3/2^-(1290)$	$M1$	0.064(24)	0.0482
		$E2$	1.9(16)	0.3
	$5/2^-(378)$	$M1$	$>0.0038^{+22}_{-10}$	0.0058
		$E2$	<0.43	1.0
	$7/2^-(0)$	$E2$	2.0(9)	4.4
$13/2^-(2563)$	$11/2^-(1441)$	$M1$	0.00146(18)	0.0022
		$E2$		0.0
$1/2^-(2671)$[a]	$5/2^-(378)$	$E2$	15(12)	2.7
$7/2^-(2686)$	$5/2^-(378)$	$M1$	0.004(4)	0.0014
		$E2$		0.1
	$7/2^-(0)$	$M1$	0.010(9)	0.0100
		$E2$	2.4(22)	0.9
$15/2^-(2693)$	$13/2^-(2563)$	$M1$	0.21(4)	0.0183
		$E2$		4.7
	$11/2^-(1441)$	$E2$	5.4(8)	3.3
$3/2^-(2876)$	$5/2^-(378)$	$M1$	$2.5\times10^{-5}(10)$	0.0040
		$E2$		0.9
	$7/2^-(0)$	$E2$	0.0008(3)	0.2
$9/2^-(2947)$	$7/2^-(0)$	$M1$	0.007(4)	0.0315
		$E2$	1.8(8)	3.9
$13/2^-(3426)$	$11/2^-(2698)$	$M1$	0.04(3)	0.0144
		$E2$	$1.6\times10^{2}(12)$	18.1
$15/2^-(3439)$	$15/2^-(2693)$	$M1$	0.23(4)	1.0585
		$E2$	$2\times10^{1}(5)$	1.3
$19/2^-(5614)$	$17/2^-(4384)$	$M1$	>0.22	0.1183
		$E2$		16.1
$21/2^-(6533)$	$17/2^-(4384)$	$E2$	2.8(16)	7.0
$23/2^-(7004)$	$21/2^-(6533)$	$M1$	0.153(24)	0.1099
		$E2$		0.0

[a] $1/2^-_2$ in the calculation.

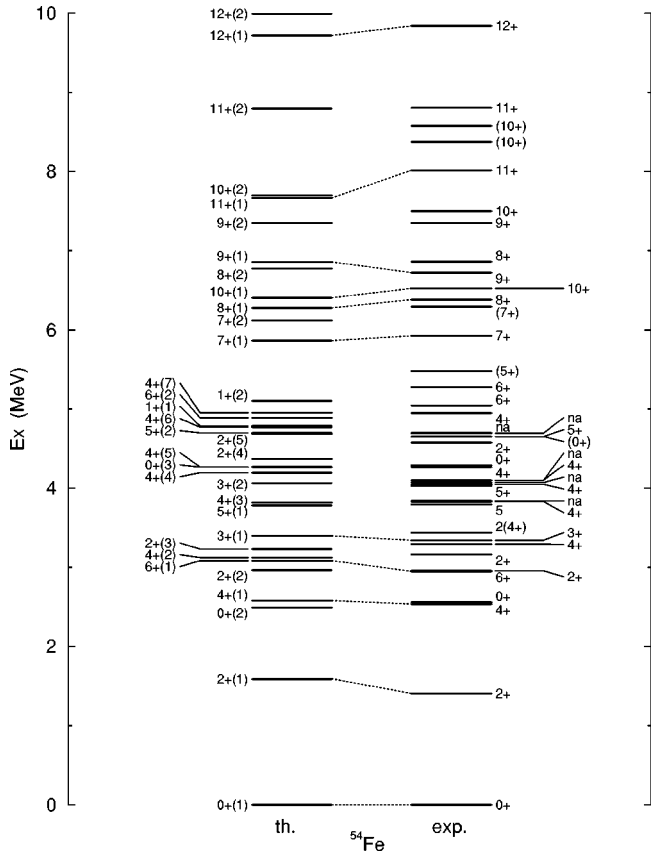

FIG. 15. Energy levels of ^{54}Fe. Experimental data are taken from Refs. [57,54]. Conventions are the same as in Fig. 14.

The yrast states up to $J^\pi = 17/2^-$ except for the ground state are described mainly by 1p-2h configurations (30–56%). Thus the truncated subspace with small $t \sim 2$ is expected to be reasonable. In fact the truncated $t=2$ subspace was used in the shell-model calculations of Ref. [54], where $13/2^-$ and higher spin states are described reasonably well. However, the excitation energies of lower spin states $9/2^-$ and $11/2^-$ are predicted to be too high by ~ 1 MeV, and the results of $5/2^-$, $3/2^-$, and $1/2^-$ are not shown in Ref. [54].

A part of such a difficulty may be attributed to the severe truncation. In the present $t=7$ results, the position of both these higher ($J^\pi \geqslant 13/2^-$) and lower spin states are successfully described. In the lower spin states, there are sizable 3p-4h ($\sim$21%) and 4p-5h ($\sim$9%) components, including both proton and neutron excitations almost equally. On the other hand, the higher spin states $13/2^-$, $15/2^-$, and $17/2^-$ are described mainly by neutron excitations only, and the probabilities of 3p-4h and 4p-5h components are much smaller ($\sim$16% and 6%, respectively). When the GXPF1 interaction is used in the $t=2$ subspace, the excitation energies of lower spin states become too large by about 0.4 MeV, while those of higher spin states are almost unchanged.

For constructing higher spin states, it is necessary to excite one more nucleon from the $f_{7/2}$ orbit. In fact the most dominant component in the wave function of these states is the 2p-3h type ($\sim$45%). A large gap ($\sim$2 MeV) between $17/2^-$ and $19/2^-$ reflects this core excitation. Note that, although it is possible to construct a $19/2^-$ state within the 1p-2h configuration space, this component is only 9% in the $19/2^-_1$ state, similar to the result in Ref. [54]. The present calculations successfully reproduce both 1p-2h and 2p-3h excitations.

The structure of nonyrast states is more complicated. Since the present interest is the low-lying core-excited states,

TABLE VIII. $B(M1)$ and $B(E2)$ for ^{54}Fe. Experimental data are taken from Ref. [57].

Initial $J^\pi(E_x)$	Final $J^\pi(E_x)$	Multipole	Expt. (W.u.)	Theor. (W.u.)
$2^+(1408)$	$0^+(0)$	$E2$	10.6(4)	10.7
$4^+(2538)$	$2^+(1408)$	$E2$	6.3(13)	5.5
$0^+(2561)$	$2^+(1408)$	$E2$	<16	3.8
$6^+(2949)$	$4^+(2538)$	$E2$	3.25(5)	3.3
$2^+(2959)$	$2^+(1408)$	$M1$	0.051(9)	0.0584
		$E2$	0.5(4)	0.2
	$0^+(0)$	$E2$	2.2(4)	3.1
$2^+(3166)$	$2^+(1408)$	$M1$	0.0035(21)	0.0013
		$E2$	1.0(13)	1.7
	$0^+(0)$	$E2$	0.74(19)	0.8
$4^+(3295)$	$4^+(2538)$	$M1$	<0.020	0.2727
		$E2$	<2.7	1.7
	$2^+(1408)$	$E2$	<0.15	0.9
$3^+(3345)$	$4^+(2538)$	$M1$	<0.0086	0.0000
		$E2$	<0.022	0.9
	$2^+(1408)$	$M1$	<0.00068	0.0004
		$E2$	<0.11	0.0
$4^+(3833)$	$4^+(3295)$	$M1$	0.011(12)	0.0312
		$E2$	$8\times10^1(9)$	1.9
	$4^+(2538)$	$M1$		0.0032
		$E2$	18(7)	0.0
	$2^+(1408)$	$E2$	7.9(18)	8.6
$4^+(4031)$[a]	$4^+(3295)$	$M1$	<0.033	0.0112
		$E2$	$<1.3\times10^2$	0.1
	$4^+(2538)$	$M1$	<0.0014	0.0514
		$E2$	<1.5	0.7
$4^+(4048)$[b]	$3^+(3345)$	$M1$	0.15(7)	0.0764
		$E2$	32^{+28}_{-24}	16.3
	$2^+(1408)$	$E2$	0.20(16)	0.3
$4^+(4268)$	$4^+(2538)$	$M1$	0.032(12)	0.0052
		$E2$	6(5)	4.8
	$2^+(1408)$	$E2$	0.60(17)	0.5
$0^+(4291)$	$2^+(1408)$	$E2$	4.3(14)	4.3
$2^+(4579)$	$2^+(1408)$	$M1$	>0.067	0.0170
		$E2$		4.9
	$0^+(0)$	$E2$	>0.99	0.7
		$M1$	0.0052(8)	0.0000
$8^+(6381)$	$6^+(2949)$	$E2$	0.86(22)	3.3
$10^+(6527)$	$8^+(6381)$	$E2$	1.69(4)	2.0

[a] 4^+_5 in the calculation.
[b] 4^+_4 in the calculation.

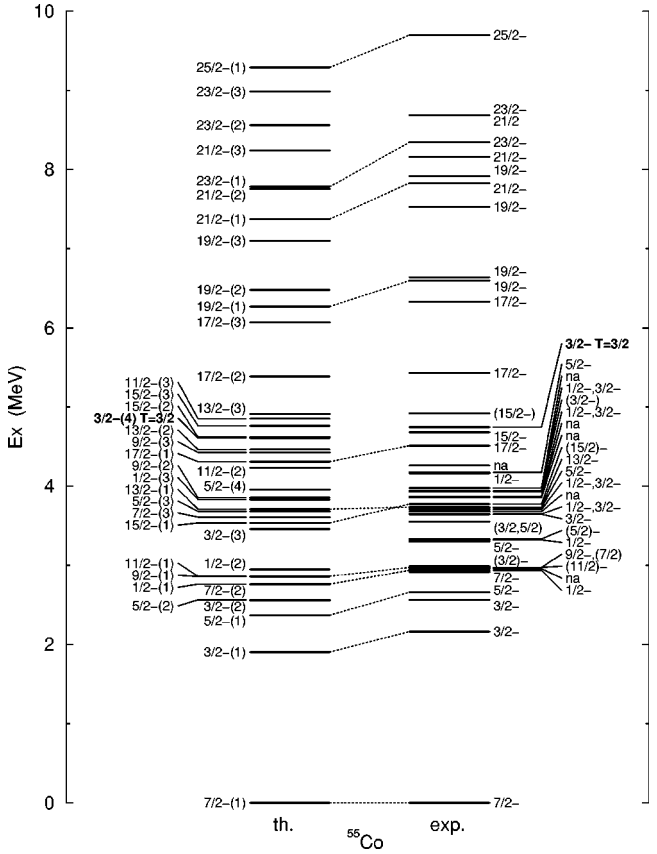

FIG. 16. Energy levels of ^{55}Co. Experimental data are taken from Refs. [58,54]. Conventions are the same as in Fig. 14.

we can focus on $1/2^-_2$, $3/2^-_3$, $7/2^-_3$, and $5/2^-_3$. These states are all below E_x=4 MeV and contain more than 45% neutron 2p-2h components. A similar character can also be seen in $3/2^-_2$, although the probability of the neutron 2p-2h component is slightly smaller (37%). These states are connected by relatively large $E2$ transition matrix elements such as $B(E2;7/2^-_3 \rightarrow 3/2^-_2)$=11 W.u. and $B(E2;5/2^-_3 \rightarrow 1/2^-_2)$ =18 W.u. It will be a good test if it is possible to observe such transitions.

The calculated $3/2^-_4$ has isospin T=3/2 and is the isobaric analog state of the ^{55}Fe ground state. The correct position of this state, as seen in comparison to experiment in Fig. 16, implies the proper isospin structure of the present interaction.

In Table IX, electromagnetic transition matrix elements are shown for ^{55}Co. We can find reasonable agreement between theory and experiment. In general, the deviations are large where the experimental errors are also large.

4. ^{56}Ni

In Fig. 17, calculated energy levels of ^{56}Ni are compared with experimental data. All calculated states up to E_x =6 MeV as well as the yrast states are shown. The shell-model results were obtained in the t=7 subspace. The agreement between the experiment and the calculation is basically good especially for even spin yrast states. However, the yrast 3^+ and 5^+ states are not found in the experimental data, while no candidate for the experimental (2^+), (4^+) and (6^+) can be

TABLE IX. $B(M1)$ and $B(E2)$ for ^{55}Co. Experimental data are taken from Ref. [58].

Initial $J^\pi(E_x)$	Final $J^\pi(E_x)$	Multipole	Expt. (W.u.)	Theor. (W.u.)
$3/2^-(2166)$	$7/2^-(0)$	$E2$	9.8(8)	8.1
$3/2^-(2566)$	$7/2^-(0)$	$E2$	1.05(25)	1.3
$1/2^-(2939)$	$3/2^-(2566)$	$M1$	0.9^{+7}_{-3}	0.1130
		$E2$		25.9
	$3/2^-(2166)$	$M1$	0.27^{+20}_{-8}	0.1371
		$E2$	34^{+48}_{-28}	0.2
$5/2^-(3303)$[a]	$7/2^-(0)$	$M1$	0.0089(20)	0.0132
		$E2$	0.15(6)	0.03
$1/2^-(3323)$	$3/2^-(2566)$	$M1$	0.47(12)	0.3100
		$E2$		7.0
	$3/2^-(2166)$	$M1$	0.17(4)	0.2514
		$E2$		9.7
$5/2^-(3725)$	$3/2^-(2566)$	$M1$	0.092(21)	0.0398
		$E2$	<0.4	0.3
	$7/2^-(0)$	$M1$	0.0055(11)	0.0263
		$E2$	0.03(3)	0.00
$1/2^-(4164)$	$3/2^-(2566)$	$M1$	0.157(20)	0.2194
		$E2$	9(3)	3.5

[a] $5/2^-_3$ in the calculation.

seen in the calculation at least around $E_x \sim 6$ MeV. More precise experimental information is needed to discuss such discrepancies. Similar results are shown in Fig. 2 of Ref. [7] for even spin states, which were obtained by the MCSM calculations, taking typically 13 bases per one eigenstate. We thus confirm the reliability of the MCSM results for nonyrast states.

For the yrast states, the ground state consists mainly of the $(f_{7/2})^{16}$ closed-shell configuration (68%). The excited states 2^+, 3^+, 4^+, 5^+, and 6^+ are of the 1p-1h character (42–50%) relative to the closed-shell configuration, and the excitation energy of 2^+_1 reflects the shell gap at N or Z=28. The 2p-2h configurations are dominant in 1^+, 7^+, 8^+, 9^+, and 10^+ states (35–51%). One can find again an energy gap between these 1p-1h and 2p-2h groups. The 3p-3h dominant states appear above $E_x \sim 10$ MeV. In the same way, most of the nonyrast excited states shown in the figure can be classified as either 1p-1h $(3^+_2, 5^+_2, \ldots)$, or 2p-2h $(2^+_2, 6^+_2, \ldots)$, dominant states. These np-nh states contain typically 20% of $(n+2)$p-$(n+2)$h configurations. Therefore, the 4p-4h configuration space is essential (but not enough) to describe these states.

As has already been discussed in Ref. [7], GXPF1 predicts the deformed 4p-4h band [60] as $0^+_3, 2^+_2, \ldots$. In the present results, 0^+_3 consists mainly of 4p-4h (48%), 5p-5h (23%), and 6p-6h (12%) configurations. The structure of 2^+_2 is quite similar. Special care should be taken concerning the convergence of the calculation for such a deformed 4p-4h band, since the present truncation scheme is obviously not suitable for describing strongly deformed states, as discussed in Ref. [13] for the case of the FPD6 interaction. Figure 18

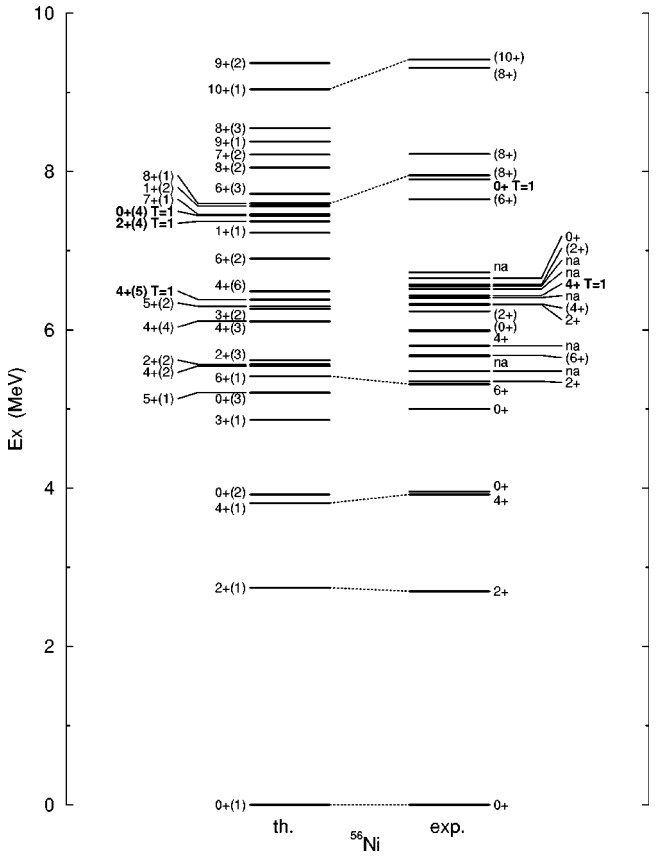

FIG. 17. Energy levels of ^{56}Ni. Experimental data are taken from Refs. [59,54]. Conventions are the same as in Fig. 14.

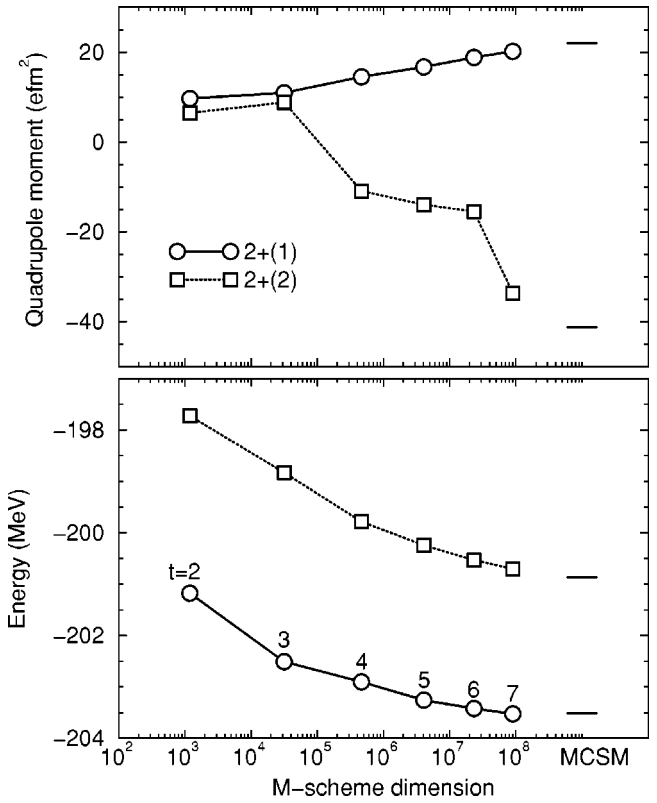

FIG. 18. Convergence of the calculated energies (lower panel) and quadrupole moments (upper panel) as functions of the truncation order t for the lowest two 2^+ states of ^{56}Ni. Horizontal lines show the corresponding MCSM results.

shows the calculated energies and quadrupole moments of the lowest two 2^+ states as a function of the truncation order t. It can be seen that the 4p-4h state 2_2^+ is not completely converged even in the $t=7$ subspace, which corresponds to the M-scheme dimension of 89 285 264. In the same figure, the MCSM results are also shown, where 25 bases were searched for each eigenstate. The MCSM energy of the yrast 2^+ state is almost the same as that of the $t=7$ calculation, which shows reasonable convergence. On the other hand, for 2_2^+ states, the MCSM energy is lower than the $t=7$ result by about 0.2 MeV, and should be more accurate. The electric quadrupole moment is $Q(2_2^+)=-41.2\ e\ \mathrm{fm}^2$ in the MCSM calculation, while it is −33.6 in the present $t=7$ result. Similar results are obtained for the 4p-4h 0_3^+ state. The M-scheme dimension of $t=8$ subspace reaches to 255 478 309, which is beyond our computational limitations. For the description of such deformed states where a lot of mixing among various spherical configurations occurs, the MCSM calculation is more efficient and suitable, because certain basis states can be sampled from and around local minima.

In the present results, we can find several $T=1$ states such as 0_4^+, 2_4^+, and 4_5^+. These states are interpreted as the isobaric analog states of ^{56}Co. The excited 0^+ with $T=1$ is in fact found experimentally at excitation energy of 7.904 MeV, which is consistent with the present result.

Experimental data for the electromagnetic transitions are rather limited. We can only compare with the few transition strengths shown in Table X.

5. ^{57}Ni

Energy levels of ^{57}Ni are shown in Fig. 19. All experimental yrast levels as well as nonyrast states up to 4 MeV excitation energy are compared with the theoretical predictions. The shell-model calculations were carried out in the $t=6$ subspace. The agreement between experiment and theory is basically good up to high spin states $23/2^-$, although there are several inversions of the order of two closely lying states, such as $7/2_1^-$ and $5/2_2^-$.

Comparing the present results with the previous MCSM ones in Ref. [7], we can again confirm the reliability of the MCSM calculations for nonyrast states as well as the yrast

TABLE X. $B(M1)$ and $B(E2)$ for ^{56}Ni. Experimental data are taken from Refs. [59,52].

Initial $J^\pi(E_x)$	Final $J^\pi(E_x)$	Multipole	Expt. (W.u.)	Theor. (W.u.)
$2^+(2701)$	$0^+(0)$	$E2$	9.4(1.9)	11.1
$4^+(3924)$	$2^+(2701)$	$E2$	<24	8.4
$6^+(5317)$	$4^+(3924)$	$E2$		5.4
$2^+(5351)$	$2^+(2701)$	$E2$		4.1
	$0^+(0)$	$E2$		0.1
$8^+(7956)$	$6^+(5317)$	$E2$		0.1
$10^+(9419)$	$8^+(7956)$	$E2$		0.1

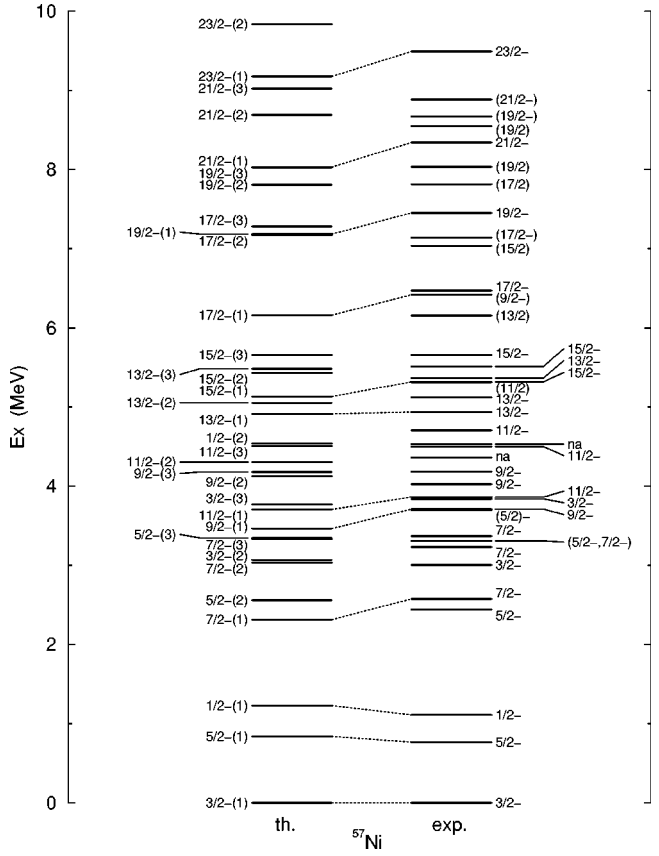

FIG. 19. Energy levels of ^{57}Ni. Experimental data are taken from Refs. [61,54]. Conventions are the same as in Fig. 14.

states of odd-mass nuclei. The root mean square difference of the excitation energies between the present and the previous MCSM results is 154 keV for 19 states shown in Fig. 2 of Ref. [7].

If we assume an inert ^{56}Ni core, ^{57}Ni is described by only one neutron. Then, three states $3/2^-$, $5/2^-$, and $1/2^-$ are possible, corresponding to the occupation of $p_{3/2}$, $f_{5/2}$, and $p_{1/2}$ orbits by one neutron. According to the present calculations, the lowest three states show such a "single-particle" character, although there is a sizable mixing of the broken-core configurations. In fact, the pure single-particle configurations are 62, 58, and 46%, respectively, in the calculated wave functions. Since the closed core configuration in the ground state of ^{56}Ni is 69% [7], the core is further broken in the ground state of ^{57}Ni, as can also be seen in Fig. 9.

The bare single-particle energy of the $f_{5/2}$ orbit relative to the $p_{3/2}$ orbit is found to be 4.3 MeV in GXPF1. (See Table I). The effective single-particle energy (ESPE) [5,11] of the $f_{5/2}$ orbit relative to the $p_{3/2}$ orbit decreases rapidly as the proton $f_{7/2}$ orbit is occupied, and reaches 1.1 MeV at ^{57}Ni. The mechanism for this behavior of the $f_{5/2}$ orbit is explained by the strong attraction between the protons in the $f_{7/2}$ orbit and neutrons in the $f_{5/2}$ orbit due to a strong $j_>$-$j_<$ coupling term in the nuclear force, as discussed in Ref. [18]. Thus the proper contribution of the two-body interaction, especially the monopole part, is needed to reproduce the experimental order of the lowest three states in ^{57}Ni. The FPD6 interaction is too strong in this respect, giving an ESPE for the $f_{5/2}$ orbit which is too low for the Ni isotopes. Note that the ESPE's of the $f_{5/2}$ and the $p_{1/2}$ orbit are still too large by 0.3 and 0.9 MeV, respectively, in comparison to the experimental excitation energies of $5/2^-$ and $1/2^-$ states, since they are defined in terms of a closed-shell structure for ^{56}Ni. Further energy gain by the mixing of the broken-core components is needed for the better reproduction of the experimental data.

TABLE XI. $B(M1)$ and $B(E2)$ for ^{57}Ni. Experimental data are taken from Ref. [61].

Initial $J^\pi(E_x)$	Final $J^\pi(E_x)$	Multipole	Expt. (W.u.)	Theor. (W.u.)
$5/2^-(769)$	$3/2^-(0)$	$M1$	0.0144(18)	0.0018
		$E2$	2.5(6)	1.4
$1/2^-(1113)$	$3/2^-(0)$	$M1$	$\leqslant 0.19$	0.1317
		$E2$	$\leqslant 3.0\times 10^2$	7.3
$5/2^-(2443)$	$3/2^-(0)$	$M1$	<0.024	0.0003
		$E2$	0.049	10.7
$7/2^-(2577)$	$3/2^-(0)$	$E2$	7.7(11)	7.4
$3/2^-(3007)$	$3/2^-(0)$	$M1$	<0.13	0.0229
		$E2$	<27	7.2
$11/2^-(3866)$	$7/2^-(2577)$	$E2$	42^{+24}_{-10}	6.8
$15/2^-(5321)^a$	$11/2^-(3866)$	$E2$	10^{+4}_{-2}	4.5

[a] $15/2^-_2$ in the calculation.

There is an energy gap ($\sim$1.3 MeV) above the lowest three states, which corresponds to the 2p-1h core excitation. The doublets $5/2^-_2$ and $7/2^-_1$ consist of two dominant configurations, $\pi(f_{7/2})^7(p_{3/2})^1\nu(f_{f7/2})^8(p_{3/2})^1$ and $\pi(f_{7/2})^8\nu(f_{f7/2})^7(p_{3/2})^2$, sharing almost equal probabilities ($\sim$20%). Above these doublets, most of the states up to $E_x \sim 5$ MeV are also of the 2p-1h nature, although one can no longer find single dominant configuration which exhausts more than 20% probability. In this 2p-1h regime, as exceptional cases, the $3/2^-_3$ and $1/2^-_2$ states comprise mainly higher configurations: the 3p-2h configuration takes the largest weight (25% and 29%, respectively) and even the 5p-4h configuration can be seen with a non-negligible probability ($\sim$5%). In the yrast $15/2^-$ and most of the higher spin states, the 3p-2h configuration becomes dominant, carrying more than 40% probability. We have not identified 4p-3h or more significantly core-broken states such as those of the deformed 4p-4h band in the ^{56}Ni in the present results for ^{57}Ni.

Electromagnetic transition strengths are shown in Table XI. Because of the large ambiguities in the experimental data, it is difficult to draw a definite conclusion. Most of the calculated $M1$ transitions are consistent with the experimental data. A notable deviation is found in the $B(M1;5/2^-_1 \rightarrow 3/2^-_1)$, where the calculated value is too small by a factor of 8. As for the $E2$ transitions, it can be seen that the calculated $B(E2)$ values are in general smaller than the experimental data. The exception is the transition from $5/2^-(2443)$. However, no experimental error is indicated in the data and only the upper bound is given for the associated $M1$ transition. The calculated $B(E2)$ value does not contradict with the experimental lifetime data.

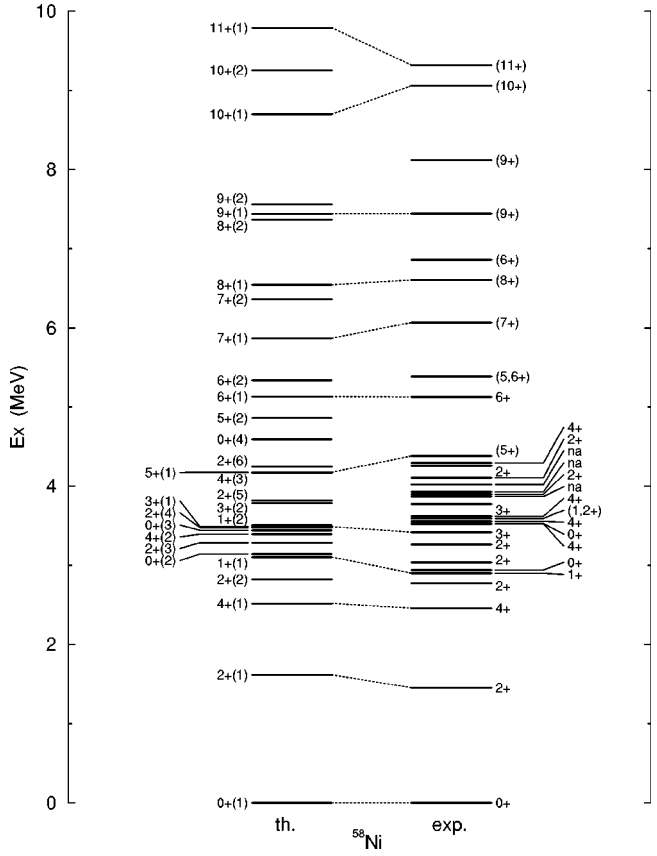

FIG. 20. Energy levels of ^{58}Ni. Experimental data are taken from Ref. [62]. Conventions are the same as in Fig. 14.

6. ^{58}Ni

Figure 20 shows calculated and experimental energy levels of ^{58}Ni. The yrast states up to 10 MeV excitation energy, nonyrast states below $E_x=4$ MeV, and several additional states are shown with their theoretical counterparts. The agreement between the experiment and the calculation is satisfactory. The calculations were carried out in the $t=6$ truncated subspace. The results are basically consistent with our previous MCSM calculations in Ref. [7], although the latter spectrum was slightly expanded for higher spin states due to the small number of basis states ($\sim$13 per one eigenstate).

In the calculated ground-state wave function, the total probability of the closed core configurations $\pi(f_{7/2})^8\nu(f_{7/2})^8(r)^2$ is only 57%, which is smaller than those in ^{56,57}Ni. As shown in Fig. 9, this quantity decreases further for larger N and takes a minimum value at $N=34$ (52%). Thus the ^{56}Ni core is soft in Ni isotopes. Nevertheless, for understanding the basic structure, it is still useful to assume an inert ^{56}Ni core and to consider two neutrons in the $p_{3/2}$, $f_{5/2}$, and $p_{1/2}$ orbits. Then, the allowed maximum spin is $J=4$, and core excitation is needed to generate higher spin states. In the calculated wave function, the leading configuration is $\nu(p_{3/2})^2$ for 0_1^+ and 2_1^+ (37% and 30%, respectively) and $\nu(p_{3/2})^1(f_{5/2})^1$ for 1_1^+ and 3_1^+ (42% and 52%, respectively). There is a large energy gap ($\sim$2 MeV) in the yrast spectrum between 4_1^+ and 5_1^+, reflecting the core excitation. One-proton core excitation dominates the wave functions up to $J=9$, although there is no single configuration which exhausts more than 20% weight in the calculated wave functions. For $J=10$ and higher spin yrast states one-proton–one-neutron core excitation becomes the most important mode. Consistently, there is another energy gap ($\sim$1.6 MeV) above 9_1^+ in both calculated and experimental energy spectra.

The closed core configurations also play a major role in many nonyrast states. Among the nonyrast states below $E_x \sim 4$ MeV, the 3p-1h configurations associated with the one-proton core excitation become dominant in 2_3^+, 4_2^+, and 3_2^+. Since the level density increases significantly above $E_x \sim 4$ MeV, it is difficult to make a simple interpretation for the properties of the core excitations in higher states.

As discussed in Ref. [7], the core excitation of two protons is dominant in the wave function of 0_3^+. In the present calculation, we found that 2_6^+ shows a similar 4p-2h character. The probability of such a 4p-2h configuration $\pi(f_{7/2})^6(r)^2\nu(f_{7/2})^8(r)^2$ is 46% and 41% for 0_3^+ and 2_6^+, respectively. The calculated quadrupole moment is $Q(2_6^+)=-0.30\ e$ b, and $B(E2;2_6^+\rightarrow 0_3^+)=18$ W.u. These values are consistent with those of the rotational model, corresponding to the $K=0$ band on top of the axially symmetric prolate rotor with an intrinsic quadrupole moment $Q_0=110\ e$ b. The deformation of the present 4p-2h band appears to be slightly smaller than the 4p-4h band in ^{56}Ni [7], which is consistent with $Q_0=140\ e$ b obtained by using the same effective charges.

In Table XII, calculated transition strengths are compared with experimental data. In general, the calculated $M1$ matrix elements are too small. The exception is $B(M1;2_2^+\rightarrow 2_1^+)$, which is too large by one order of magnitude. As for the $E2$ matrix elements, the calculated values are almost consistent with experimental data in the case of $\Delta J=2$ transitions, i.e., no mixing of $M1$ transitions. One notable exception is $B(E2;0_2^+\rightarrow 2_1^+)$, which is too large by more than three orders of magnitude, but this is an extremely weak transition.

7. ^{59}Ni

Energy levels of ^{59}Ni are shown in Fig. 21. All experimental data for yrast states as well as nonyrast states below 3 MeV excitation energy are compared with the shell-model results obtained in the $t=6$ subspace. It is found that the theoretical results agree quite well with the experimental data. The results of the lowest triplet $3/2^-$, $5/2^-$, and $1/2^-$ have already been reported in Ref. [7]. The present calculation has confirmed the validity of GXPF1 interaction also for higher excited states.

Assuming an inert ^{56}Ni core, this nucleus is described by three valence neutrons in the upper three orbits $p_{3/2}$, $f_{5/2}$, and $p_{1/2}$. Therefore various states are possible without any core excitation. In fact such closed-shell (3p-0h) configurations carry the maximum weight (31–56%) in most of the calculated low-lying states below $E_x=3$ MeV. There are three exceptions, $7/2_2^-$, $7/2_3^-$, and $11/2_1^-$, where 4p-1h configurations take the largest weight. Such 4p-1h configurations also dominate the wave functions of higher-lying excited states shown in the same figure. The 5p-2h configurations appear to be the leading configurations in the yrast $19/2^-$ and $21/2^-$ states.

TABLE XII. $B(M1)$ and $B(E2)$ for ^{58}Ni. Experimental data are taken from Ref. [62].

Initial $J^\pi(E_x)$	Final $J^\pi(E_x)$	Multipole	Expt. (W.u.)	Theor. (W.u.)
$2^+(1454)$	$0^+(0)$	$E2$	9.8(5)	7.7
$4^+(2459)$	$2^+(1454)$	$E2$	<43	4.1
$2^+(2775)$	$2^+(1454)$	$M1$	0.011(4)	0.1103
		$E2$	15(5)	1.2
	$0^+(0)$	$E2$	0.029(10)	2.8
$0^+(2942)$	$1^+(2902)$	$M1$	0.084(6)	0.0068
	$2^+(2775)$	$E2$	14.9(18)	12.4
	$2^+(1454)$	$E2$	0.00029(4)	0.63
$2^+(3038)$	$2^+(2775)$	$M1$	0.23(6)	0.0275
		$E2$	6^{+20}_{-6}	1.0
	$2^+(1454)$	$M1$	0.060(12)	0.0190
		$E2$	2.0(7)	15.0
$2^+(3263)$	$2^+(1454)$	$M1$	0.028(11)	0.0004
		$E2$	8(7)	0.01
$3^+(3420)$	$4^+(2459)$	$M1$	0.09(8)	0.1101
		$E2$	0.07^{+23}_{-7}	0.11
$0^+(3531)$	$2^+(1454)$	$E2$	5.5	3.5
$4^+(3620)$	$4^+(2459)$	$M1$	0.07^{+7}_{-4}	0.0002
		$E2$	44^{+60}_{-36}	1.3
	$2^+(1454)$	$E2$	1.4^{+12}_{-6}	6.7
$3^+(3774)$	$3^+(3420)$	$M1$	0.33(17)	0.0169
		$E2$	$(1\times10^1)^{+11}_{-1}$	0.1
	$4^+(2459)$	$M1$	0.019(10)	0.0001
		$E2$	0.8^{+12}_{-8}	0.4
$2^+(3898)$	$2^+(1454)$	$M1$	0.042^{+25}_{-11}	0.0410
	$0^+(0)$	$E2$	0.42^{+25}_{-11}	0.81
$2^+(4108)$	$2^+(2775)$	$M1$	0.0051(20)	0.0089
	$2^+(1454)$	$M1$	0.0032(8)	0.0003
		$E2$	0.30(10)	0.29
	$0^+(0)$	$E2$	0.15(4)	0.08

Like other nuclei, we would like to identify states with large components of 5p-2h or higher configurations at $E_x < \sim 3$ MeV. This energy boundary is set because the level density increases very fast above it in ^{59}Ni. However, as seen from the above discussions, there are no such candidate states theoretically or experimentally. Therefore, the study of 5p-2h and higher states with lower angular momenta is not possible in ^{59}Ni. Thus, the discussion of the multiparticle multihole states which is one of the main elements in our assessment of the effective interaction is confined mainly to a few nuclei around ^{56}Ni.

Table XIII shows the measured and calculated $B(E2)$ and $B(M1)$. Even below $E_x=2$ MeV, there are several uncertain levels in the experimental data at 1695 keV (no spin assignment), 1739 keV [assigned to $(9/2^-)$], and 1746 keV (assigned to $5/2^-$, $7/2^-$). In the present calculations, we have tentatively assigned no theoretical states to these three uncertain states, since no probable candidates appear around E_x

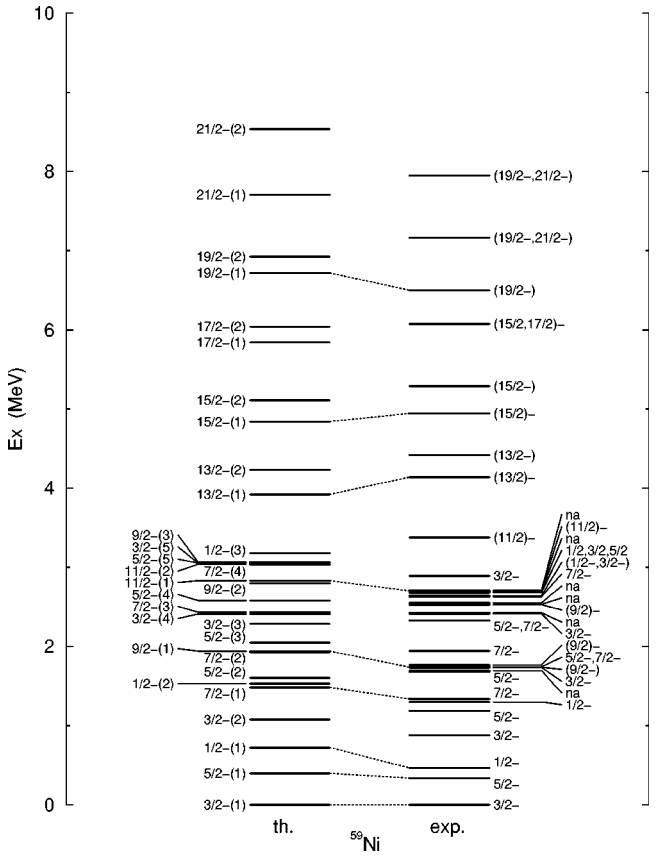

FIG. 21. Energy levels of ^{59}Ni. Experimental data are taken from Ref. [63]. Conventions are the same as in Fig. 14.

~ 2 MeV. More experimental information is needed for a detailed comparison between theory and experiment.

In general, the order of magnitude is well reproduced for most transitions. More specifically, the calculated $M1$ transition matrix elements are small in comparison to the experimental data in many cases, except for $1/2^-_1 \rightarrow 3/2^-_1$ transition. The calculated $E2$ matrix elements are also smaller than the experimental data. However, one can clearly see the correlation between the calculated values and the corresponding experimental data. The agreement could be improved if we introduced larger effective charges.

G. $N=Z$ odd-odd nuclei

In the pf shell, $N=Z$ odd-odd nuclei have been of special interest, where the lowest isospin $T=0$ and $T=1$ states are almost degenerate near the ground state. In most cases $T=1$, $J=0$ is the ground state. The only known exception is ^{58}Cu, in which the ground state is $T=0$, $J=1$. This reflects a detailed interplay of $T=0$ and $T=1$ interactions, and it is important to evaluate the effective interaction from this viewpoint.

1. ^{54}Co

In Fig. 22, calculated energy levels of ^{54}Co are compared with experimental data. The spin-parity has not been assigned to most of the states above $E_x=3$ MeV, and there are

TABLE XIII. $B(M1)$ and $B(E2)$ for ^{59}Ni. Experimental data are taken from Ref. [63].

Initial $J^\pi(E_x)$	Final $J^\pi(E_x)$	Multipole	Expt. (W.u.)	Theor. (W.u.)
$5/2^-(339)$	$3/2^-(0)$	$M1$	0.0083(10)	0.0031
		$E2$		0.26
$1/2^-(465)$	$3/2^-(0)$	$M1$	0.011(2)	0.0705
		$E2$		1.7
$3/2^-(878)$	$3/2^-(0)$	$M1$	0.068(13)	0.0327
		$E2$	1.1(9)	7.0
$5/2^-(1189)$	$3/2^-(0)$	$M1$	0.043(9)	0.0058
		$E2$	11(5)	10.1
$1/2^-(1301)$	$1/2^-(465)$	$M1$	0.036(8)	0.0016
	$5/2^-(339)$	$E2$	1.2(4)	0.4
$7/2^-(1338)$	$5/2^-(339)$	$M1$	0.0008(3)	0.0002
		$E2$	30(7)	10.7
	$3/2^-(0)$	$E2$	2.9(7)	0.8
$5/2^-(1680)$	$1/2^-(465)$	$E2$	1.41(23)	0.20
	$3/2^-(0)$	$M1$	0.0009(7)	0.0095
		$E2$	1.6(5)	1.1
$9/2^-(1768)$	$7/2^-(1338)$	$M1$	0.042(11)	0.0210
		$E2$	4^{+5}_{-3}	1.8
	$5/2^-(339)$	$E2$	11(3)	3.3
$7/2^-(1948)$	$5/2^-(1189)$	$M1$	0.042(9)	0.0368
		$E2$	10(10)	0.9
	$3/2^-(878)$	$E2$	3.6(10)	2.7
	$3/2^-(0)$	$E2$	5.3(10)	7.2
$11/2^-(2705)$	$9/2^-(1768)$	$M1$	0.0040(13)	0.0005
		$E2$	8(3)	1.7
	$7/2^-(1338)$	$E2$	22(6)	4.5

several uncertain levels among low-lying states. It can be seen that the present shell-model calculations in the $t=6$ subspace give a reasonable description, although there are several small deviations such as the interchange of the order of 2^+_1 and 3^+_1. The calculated $0^+_{1,2}$, 2^+_1, $4^+_{3,4}$, and 6^+_2 are $T=1$, corresponding to the isobaric analog states of ^{54}Fe (see Fig. 15), while other calculated states shown in the figure are $T=0$.

In the calculated wave functions of the yrast odd-spin states 1^+_1, 3^+_1, 5^+_1, and 7^+_1, the lowest $\pi(f_{7/2})^7\nu(f_{7/2})^7$ configuration is dominant (59%, 58%, 39%, and 62%, respectively), but core-excited components are not small. Such lowest 0p-2h configurations relative to ^{56}Ni core are also dominant in even-spin 0^+_1, 2^+_1, 4^+_3, and 6^+_2, which are all $T=1$.

In the shell-model calculations [64] using the surface delta interaction in the $(f_{7/2},p_{3/2})$ space with a restriction that the $p_{3/2}$ orbit can be occupied by one proton and one neutron, the 4^+ and 6^+ states of $T=1$ appear as yrast states. On the other hand, $4^+_{1,2}$ are isospin $T=0$ in the present calculation. If the calculated 4^+_1 is assigned to the experimental state $(3^+,4^+)$ at 2083 keV, the agreement between theory and experiment is good. This state consists mainly of the 1p-3h configurations (50%). A similar structure can be seen for 6^+_1,

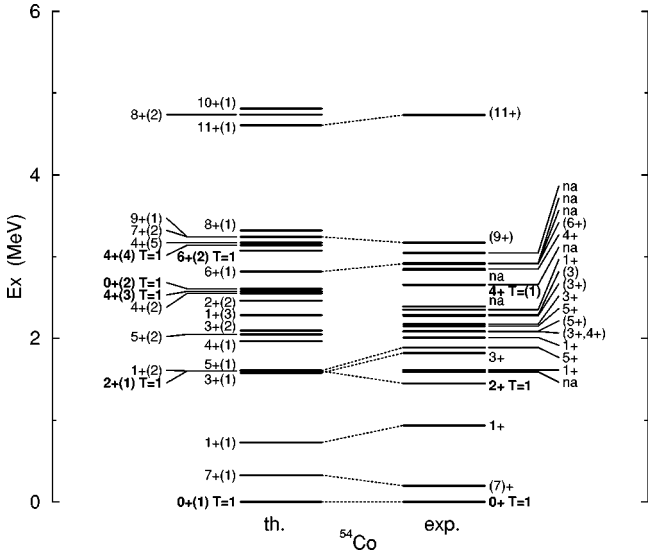

FIG. 22. Energy levels of ^{54}Co. Experimental data are taken from Refs. [65,54]. Conventions are the same as in Fig. 14.

5^+_2, 7^+_2, and $8^+_{1,2}$, where one nucleon is excited across the shell gap mainly to the $p_{3/2}$ orbit. The structure of 4^+_2 is similarly of the 1p-3h type, although the excitation to the $f_{5/2}$ orbit is dominant. Such an excitation is also large in 8^+_2.

One can find a 1^+_2 state in the calculated spectra at a reasonable excitation energy, which does not appear in the shell-model results of Ref. [64]. The most important configuration in this state is $\pi(f_{7/2})^6(p_{3/2})^1\nu(f_{7/2})^6(p_{3/2})^1$, but its probability is only 15%. Such 2p-4h configurations are 44% in total, and there are other sizable core-excited components such as the 3p-5h (32%) and 4p-6h (17%) types. Similar core excitations also appear in 2^+_2, 3^+_2, and 0^+_2 $(T=1)$.

The calculated $M1$ and $E2$ transition strengths are listed in Table XIV. Since no experimental value is available, the present results are compared with those of the shell-model calculation in Ref. [64]. Both results agree within a factor of about 2 for transitions between the states which consist mainly of the 0p-2h configurations. The strong isovector $M1$ transitions predicted based on the "quasideuteron" picture [66] are found also in the present large-scale calculations. Note that the effective spin g factors $g_s^{\rm eff}=0.7g_s^{\rm free}$ were used in Ref. [64]. If we adopt the same g factors in the present calculations, the $B(M1)$ values are significantly reduced, for example, $B(M1;1^+_1\rightarrow 0^+_1)$ becomes 1.25 W.u. Thus the configuration mixing strongly affects the $B(M1)$ value.

Several results related to the 1^+ (1614), 3^+ (2174), and 4^+ (2852) states are very different between two calculations, because the structure of the corresponding states are different as mentioned above.

2. ^{58}Cu

In Fig. 23, the calculated energy levels of ^{58}Cu are compared with experimental data. All experimental states up to 2.2 MeV as well as the yrast states are shown. The shell-model calculations have been carried out in the $t=6$ truncated subspace. The agreement between theory and experiment is satisfactory. In the calculated spectrum, 0^+_1, 2^+_2, 4^+_3,

TABLE XIV. $B(M1)$ and $B(E2)$ for ^{54}Co.

Initial $J^\pi(E_x)$	Final $J^\pi(E_x)$	Multipole	Th-2. of Ref. [64] (W.u.)	Theor. (W.u.)
$1^+(937)$	$0^+(0)$	$M1$	2.13	1.90
$2^+(1446)$	$1^+(937)$	$M1$	2.33	2.36
		$E2$	0.033	0.078
	$0^+(0)$	$E2$	10.6	7.7
$3^+(1822)$	$2^+(1446)$	$M1$	2.36	1.92
		$E2$	0.091	0.155
	$1^+(937)$	$E2$	10.6	4.2
$3^+(2174)$	$2^+(1446)$	$M1$	0.016	0.0055
		$E2$	0.0012	0.0000
	$1^+(1614)$	$E2$	1.1	16.0
	$1^+(937)$	$E2$	0.29	0.06
$4^+(2652)^a$	$3^+(1822)$	$M1$	2.00	1.95
		$E2$	0.18	0.39
	$2^+(1446)$	$E2$	7.8	3.6
	$5^+(1887)$	$M1$	2.13	1.07
		$E2$	0.21	0.29
$4^+(2852)^b$	$3^+(1822)$	$M1$	0.002	0.0000
		$E2$	0.12	0.02
	$5^+(1887)$	$M1$	0.004	0.0000
		$E2$	7.1	0.03

[a] 4_3^+ in the calculation.
[b] 4_2^+ in the calculation.

and 0_2^+ are isospin $T=1$. The $T_z=1$ members of the multiplets can in fact be seen in the calculated spectrum of ^{58}Ni (see Fig. 20). The $T=0$ ground state 1_1^+ is successfully reproduced.

Assuming an inert ^{56}Ni core, one proton and one neutron are valence particles in the $p_{3/2}$, $f_{5/2}$, and $p_{1/2}$ orbits. Therefore $J \leqslant 5$ states are possible. In the calculated wave functions, the yrast states up to 5^+ are in fact dominated by such closed core configurations with probabilities of 44–63%. The 6_1^+ state consists mainly of 3p-1h configurations (45%). The 4p-2h configurations are dominant in 7_1^+, 8_1^+, 9_1^+, and 10_1^+ (41–59%), and the 5p-3h configurations become the major components in 11_1^+ and 12_1^+ ($\sim$40%). Thus it is natural that the $t=2$ shell-model results in Ref. [54] show apparent discrepancies from experiment for 11^+ and 12^+.

In the present calculation, all states with $J \leqslant 10$ are dominated by either 3p-1h or 4p-2h configurations. Therefore, shell-model calculations even in the severely truncated ($t \sim 2$) subspace give reasonable results at least near the yrast line. In order to obtain further information on the core excitation, it is necessary to study higher spin states or highly excited states far from the yrast line. From this viewpoint, recent precise measurements [68] of the Gamow-Teller strength distribution in this nucleus up to high excitation energy provide quite important information. The GXPF1 reproduces the measured strengths around $E_x \sim 4$ MeV reasonably well, which are missing in the prediction of the KB3G interaction.

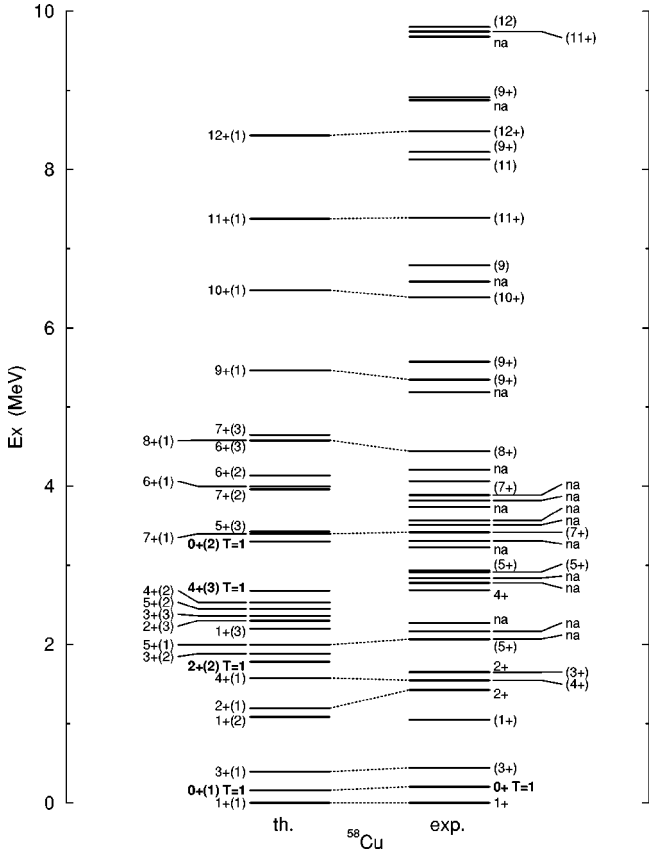

FIG. 23. Energy levels of ^{58}Cu. Experimental data are taken from Refs. [67,54]. Conventions are the same as in Fig. 14.

In the calculated wave function of the ground state 1_1^+, the configuration $\pi(p_{3/2})^1\nu(p_{3/2})^1$ takes the largest weight (18%) and the second largest components are $\pi(p_{3/2})^1\nu(p_{1/2})^1$ and $\pi(p_{1/2})^1\nu(p_{3/2})^1$ (13% for each). This is not very far from the quasideuteron picture [66], although the configuration $\pi(p_{3/2})^1\nu(p_{3/2})^1$ is distributed among several 1^+ states such as 1_2^+ (15%) and 1_3^+ (20%). However, it contradicts with the shell-model results in Ref. [54], where $\pi(p_{3/2})^1\nu(f_{5/2})^1$ and $\pi(f_{5/2})^1\nu(p_{3/2})^1$ are dominant (20% for each).

The calculated $B(M1)$ and $B(E2)$ values are compared with experimental data in Table XV. Although the experi-

TABLE XV. $B(M1)$ and $B(E2)$ for ^{58}Cu. Experimental data are taken from Refs. [70,67].

Initial $J^\pi(E_x)$	Final $J^\pi(E_x)$	Multipole	Expt. (W.u.)	Theor. (W.u.)
$0^+(203)$	$1^+(0)$	$M1$		0.8473
$1^+(1051)$	$0^+(203)$	$M1$	0.46(10)	0.1358
$2^+(1652)$	$0^+(203)$	$E2$	14.8(37)	10.2
	$3^+(444)$	$M1$	0.33(11)	0.5220
		$E2$		0.1
	$1^+(1051)$	$M1$	0.17(6)	0.1780
		$E2$		0.0

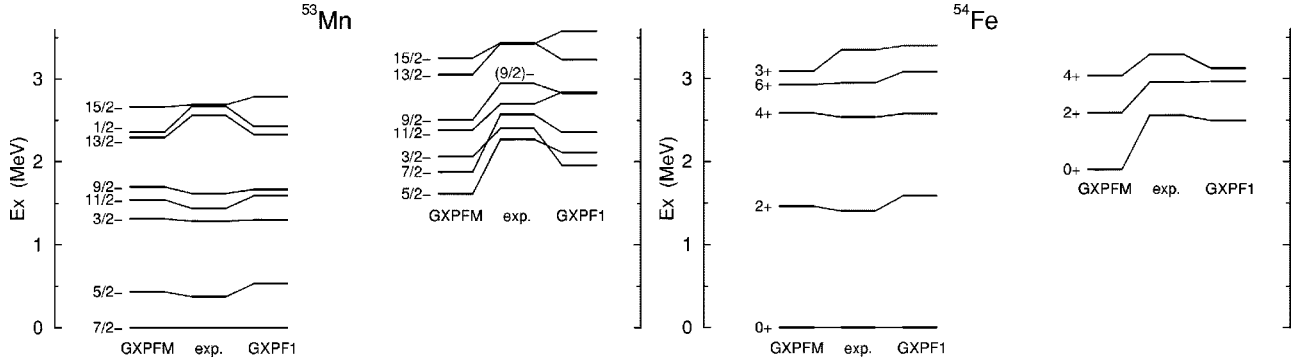

FIG. 24. Comparison of low-lying energy levels of (left) ^{53}Mn and (right) ^{54}Fe between the experimental data and the shell-model predictions by GXPFM and GXPF1.

mental data are limited, the agreement between theory and experiment is reasonable. More detailed discussions are found in Ref. [69].

H. GXPF1 versus GXPFM

In the previous sections, it has been shown that GXPF1 properly describes the low-lying core excitations. As discussed above, the effects of the core excitations can be observed directly in the low-lying energy spectra of semimagic nuclei, and therefore the description of such core-excited states plays a crucial role for the evaluation of the effective interaction. From this viewpoint, in this section, we discuss a specific problem with the GXPFM interaction: an interaction derived by adding empirical corrections to the microscopic G interaction only in the monopole part and pairing matrix elements (see Sec. II F). With the FDA* estimate, the description of energy data by GXPFM appears to be poor especially for the yrare states of semimagic nuclei.

As examples, we consider the low-lying energy levels of ^{53}Mn and ^{54}Fe, which are shown in Fig. 24 for yrast and yrare states. Details of the shell-model calculations are the same as those described in Sec. III F. For a comparison, the results of GXPF1 are also shown. It can be clearly seen that, in both nuclei, the yrast states are described nearly equally well by both GXPF1 and GXPFM at least in the region of $E_x \leqslant 3.5$ MeV. On the other hand, several yrare states such as $5/2_2^-$ and $7/2_2^-$ in ^{53}Mn and 0_2^+ in ^{54}Fe are predicted to be too low by GXPFM. According to the analysis of the shell-model wave functions, these states are dominated by neutron core-excited configurations. Typically 40% of these wave functions consist of neutron 2p-2h configurations relative to the $N=28$ core. In the case of GXPF1, such states are predicted with a similar structure, while their excitation energies are closer to the experiment.

This fact suggests that the "monopole + pairing" correction works well for the description of the states in the lowest configuration and those with 1p-1h excitations relative to it, but it is not sufficient for treating the states which are dominated by the 2p-2h or more excited configurations. This is natural because, in the former states, the structure is expected to be single-particle-like, especially for the semimagic nuclei, and therefore such states can be described well by adjusting the monopole part only. On the other hand, in the latter states, the contribution of the multipole part should be more important, and multipole parts must be modified for their proper descriptions. Thus, the core excitations provide us with a clue to investigate corrections to the interaction that go beyond monopole plus pairing.

I. Quadrupole corrections

In Sec. II B, it has been shown that major modifications of the microscopic interaction can be found in the diagonal parts which are not necessarily of monopole character. We have also shown in the preceding section that the monopole + pairing correction is insufficient for describing the property of core excitations. Such insufficiency can be seen explicitly in the energy spectra of semimagic nuclei.

Figure 25 shows a part of the low-lying energy levels of ^{56}Ni and ^{57}Ni, where the results of GXPF1, GXPFM, and KB3G are compared. The latter two interactions predict too

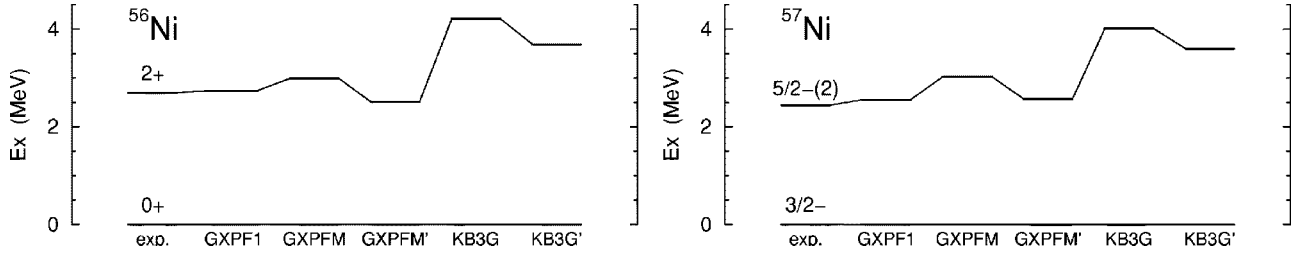

FIG. 25. Comparison of the excitation energy of (left) 2_1^+ in ^{56}Ni and (right) $5/2_2^-$ in ^{57}Ni between the experimental data and the results of various effective interactions. The shell-model calculations were carried out in the $t=7$ and 6 truncated subspaces for ^{56}Ni and ^{57}Ni, respectively.

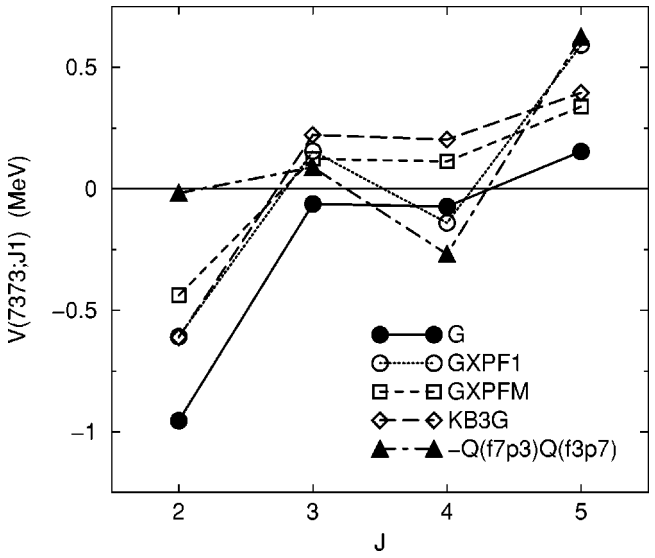

FIG. 26. Comparison of two-body matrix elements $V(7373;J1)$ between various effective interactions.

high excitation energies for the 2_1^+ state in ^{56}Ni and the $5/2_2^-$ state in ^{57}Ni. Both of these excited states are dominated by the configuration with one nucleon excited from the $f_{7/2}$ orbit to the $p_{3/2}$ orbit.

We have found that in this case the most relevant matrix elements are $V(7373;J1)$, which are compared in Fig. 26 for G, GXPF1, GXPFM, and KB3G. It can be seen that the difference between G and GXPFM is primarily of monopole character (constant shift). Similar monopole corrections are present in KB3G, although its original microscopic interaction is not G but KB, reflecting that G and KB are very close for these matrix elements. On the other hand, GXPF1 shows a rather different J dependence from these "monopole-corrected" interactions GXPFM and KB3G, especially for the $J=4$ and $J=5$ matrix elements. The former is more attractive and the latter more repulsive by about 0.3 MeV. Note that these differences keep the monopole centroid of quite similar value for these interactions as shown in Figs. 2 and 8.

In order to examine to what extent such differences affect the energy spectra, similar calculations have been carried for both GXPFM and KB3G interactions, by modifying the $J=4$ matrix element to be more attractive by 0.300 MeV and $J=5$ to be more repulsive by 0.245 MeV so that the monopole centroid is kept unchanged. The modified interactions are denoted as GXPFM′ and KB3G′, respectively. The results are shown in Fig. 25. It is clearly seen that the description is improved in both GXPFM′ and KB3G′, although it is not enough for the latter. This fact highlights the importance of modifications of the microscopic interaction that go beyond the monopole type.

The above J-dependent modifications in GXPF1 can be understood to a good extent in terms of a quadrupole-quadrupole interaction $[(f_{7/2})^\dagger(\tilde{p}_{3/2})]^{(2)}\cdot[(p_{3/2})^\dagger(\tilde{f}_{7/2})]^{(2)}$. The matrix elements of this interaction are shown in Fig. 26, which give similar J dependence to that of the difference between GXPF1 and GXPFM. Indeed, the $V(7373;J1)$'s can be obtained by recoupling this interaction with the strength −0.81 MeV for GXPF1 together with other multipoles with minor contributions, while this strength turns out to be −0.32, −0.34, and −0.38 MeV for GXPFM, KB3G, and G, respectively. This quadrupole correction can arise from a core-polarization diagram where the external lines are $f_{7/2}$ and $p_{3/2}$ with exchange between them and the bubble of $J^\pi=2^+$ is involved. If this is the case, the coupling should be particularly strong in this channel and/or the energy denominator should be smaller, as compared to what is assumed in the microscopic calculation of effective interaction. This is an intriguing problem of the effective interaction, and further studies are needed.

IV. SUMMARY

Summarizing this paper, the effective interaction for pf-shell nuclei, GXPF1, has been examined and tested from various viewpoints. It was obtained by adding empirical corrections to the microscopic interaction derived from the nucleon-nucleon potential. The corrections were determined through the systematic fitting to experimental energy data. The most significant modifications are those for the monopole and pairing parts of the Hamiltonian. The monopole plus pairing corrections give a substantial improvement, but are not sufficient for the description core excitations over the N or $Z=28$ shell gap. Other modifications are necessary including some which can be related to the quadrupole-quadrupole component.

The analysis of the ground-state wave functions obtained by GXPF1 shows that the assumption of an inert ^{56}Ni core is not realistic even for the Ni isotopes. Thus, the amount of core excitations strongly depends on both valence proton and neutron numbers relative to the core.

The calculated binding energies agree with the experimental data quite well over a wide mass range even for many nuclei which were not included in the fit. However, in neutron-rich nuclei ($N>34$) around $Z\sim24$, the difference between theory and experiment becomes larger, suggesting a need for including the $g_{9/2}$ orbit for describing large deformation. Such a discrepancy can also be seen in the calculated 2_1^+ excitation energy for ^{60}Cr, which is predicted too high in comparison to the recent experimental data.

The description of the magnetic dipole and electric quadrupole moments is basically successful with a few exceptions. The most remarkable difference between theory and experiment can be found in the 2_1^+ states of Zn isotopes, which also suggests influence of the $g_{9/2}$ orbit. As for the electric quadrupole moments, more precise experimental data are desired to discuss the quality of description especially for Ni and Zn isotopes.

The energy spectra and electromagnetic transition matrix elements for N or $Z=28$ semimagic nuclei have been calculated and compared with experimental data. The effects of the core excitation across N, $Z=28$ shell gap can be seen already in the nonyrast states around $E_x\sim3$ MeV as well as high spin yrast states. The present results show the reliability of GXPF1 even in the cases in which the core excitation plays a crucial role. Considering the current experimental

and theoretical situations, it would be difficult to explore such significantly core-excited states in other nuclei with more "valence" particles or holes relative to ^{56}Ni core, due to the explosive increase of the low-lying level density. Therefore the description of ^{56}Ni and neighboring nuclei is an important test of the effective interaction.

It has been shown that the reasonable description of $N=Z$ odd-odd nuclei can be obtained by GXPF1, indicating its proper isospin dependent structure, although the experimental data are limited especially for the transitions.

Most of shell-model calculations were done in the conventional method so as to reach higher accuracy. The truncations were carefully examined to be accurate enough and for the data we compare with. In some shape coexistence cases, strongly deformed states appear at lower energies, where the Monte Carlo shell model still produces more accurate results as compared to large-scale conventional calculations with high (i.e., unrestrictive) truncations. Thus, one has to be cautious in using conventional calculations for such cases. This may be an important lesson for further studies on heavier nuclei with more developed collectivity.

Further applications to unexplored regimes of large proton/neutron numbers or high excitation energy are of great interest. Future experiments will test the predictions and provide guidance for further improvements in the interaction.

ACKNOWLEDGMENTS

This work has been supported in part by Grant-in-Aid for Specially Promoted Research (Grant No. 13002001) from the Japanese Ministry of Education, Science, Culture, Sport and Technology. Shell-model calculations were performed largely on the parallel computer system at CNS and on the Alphleet computer of RIKEN. The CNS system has been installed by the above-mentioned grant, and these computers are operated under the joint large-scale nuclear-structure calculation project by RIKEN and CNS. B.A.B. acknowledges support from NSF Grant Nos. PHY-0244453 and INT-0089581.

[1] T. Otsuka, M. Honma, and T. Mizusaki, Phys. Rev. Lett. **81**, 1588 (1998).
[2] T. T. S. Kuo and G. E. Brown, Nucl. Phys. **A114**, 241 (1968).
[3] M. Hjorth-Jensen, T. T. S. Kuo, and E. Osnes, Phys. Rep. **261**, 125 (1995).
[4] J. B. McGrory, B. H. Wildenthal, and E. C. Halbert, Phys. Rev. C **2**, 186 (1970).
[5] A. Poves and A. P. Zuker, Phys. Rep. **70**, 235 (1981).
[6] A. Poves, J. Sánchez-Solano, E. Caurier, and F. Nowacki, Nucl. Phys. **A694**, 157 (2001).
[7] M. Honma, T. Otsuka, B. A. Brown, and T. Mizusaki, Phys. Rev. C **65**, 061301(R) (2002).
[8] S. Cohen and D. Kurath, Nucl. Phys. **73**, 1 (1965).
[9] B. A. Brown and B. H. Wildenthal, Annu. Rev. Nucl. Part. Sci. **38**, 29 (1988).
[10] M. Honma, T. Mizusaki, and T. Otsuka, Phys. Rev. Lett. **75**, 1284 (1995); **77**, 3315 (1996).
[11] Y. Utsuno, T. Otsuka, T. Mizusaki, and M. Honma, Phys. Rev. C **60**, 054315 (1999).
[12] Y. Utsuno, T. Otsuka, T. Mizusaki, and M. Honma, Phys. Rev. C **64**, 011301(R) (2001).
[13] T. Mizusaki, T. Otsuka, M. Honma, and B. A. Brown, Nucl. Phys. **A704**, 190c (2002).
[14] N. Shimizu, T. Otsuka, T. Mizusaki, and M. Honma, Phys. Rev. Lett. **86**, 1171 (2001).
[15] M. Honma, B. A. Brown, T. Mizusaki, and T. Otsuka, Nucl. Phys. **A704**, 134c (2002).
[16] W. Chung, Ph.D. thesis, Michigan State University, 1976.
[17] B. A. Brown, W. A. Richter, R. E. Julies, and H. B. Wildenthal, Ann. Phys. (N.Y.) **182**, 191 (1988).
[18] T. Otsuka *et al.*, Phys. Rev. Lett. **87**, 082502 (2001).
[19] T. Otsuka, Prog. Theor. Phys. Suppl. **146**, 6 (2003).
[20] T. Suzuki, R. Fujimoto, and T. Otsuka, Phys. Rev. C **67**, 044302 (2003).
[21] M. Dufour and A. P. Zuker, Phys. Rev. C **54**, 1641 (1996).
[22] W. Satuła and R. Wyss, Phys. Lett. B **393**, 1 (1997).
[23] T. Otsuka, A. Arima, F. Iachello, and I. Talmi, Phys. Lett. **76B**, 139 (1978).
[24] T. Otsuka, A. Arima, and F. Iachello, Nucl. Phys. **A309**, 1 (1978).
[25] J. Dobaczewski, W. Nazarewicz, J. Skalski, and T. Werner, Phys. Rev. Lett. **60**, 2254 (1988).
[26] W. A. Richter, M. G. van der Merwe, R. E. Julies, and B. A. Brown, Nucl. Phys. **A523**, 325 (1991).
[27] M. G. van der Merwe, W. A. Richter, and B. A. Brown, Nucl. Phys. **A579**, 173 (1994).
[28] T. Mizusaki, T. Otsuka, Y. Utsuno, M. Honma, and T. Sebe, Phys. Rev. C **59**, R1846 (1999).
[29] T. Mizusaki, T. Otsuka, M. Honma, and B. A. Brown, Phys. Rev. C **63**, 044306 (2001).
[30] T. Mizusaki, RIKEN Accel. Prog. Rep. **33**, 14 (2000).
[31] K. Langanke, D. J. Dean, P. B. Radha, Y. Alhassid, and S. E. Koonin, Phys. Rev. C **52**, 718 (1995).
[32] E. Caurier, G. Martinez-Pinedo, F. Nowacki, A. Poves, J. Retamosa, and A. P. Zuker, Phys. Rev. C **59**, 2033 (1999).
[33] G. Audi and A. H. Wapstra, Nucl. Phys. **A595**, 409 (1995).
[34] A. Huck *et al.*, Phys. Rev. C **31**, 2226 (1985).
[35] B. A. Brown, Prog. Part. Nucl. Phys. **47**, 517 (2001).
[36] G. Martinez-Pinedo, A. Poves, E. Caurier, and A. P. Zuker, Phys. Rev. C **53**, R2602 (1996).
[37] Data extracted using the NNDC World Wide Web site from the ENSDF database.
[38] R. Ernst *et al.*, Phys. Rev. Lett. **84**, 416 (2000).
[39] K.-H. Speidel *et al.*, Phys. Rev. C **62**, 031301(R) (2000).
[40] S. Wagner *et al.*, Phys. Rev. C **64**, 034320 (2001).
[41] T. Ohtsubo *et al.*, Phys. Rev. C **54**, 554 (1996).
[42] O. Kenn *et al.*, Phys. Rev. C **63**, 021302(R) (2000).
[43] O. Kenn *et al.*, Phys. Rev. C **65**, 034308 (2002).
[44] P. Dufek, P. Blaha, and K. Schwarz, Phys. Rev. Lett. **75**, 3545 (1995).

[45] M. Hass *et al.*, Nucl. Phys. **A414**, 316 (1984).
[46] R. V. F. Janssens *et al.*, Phys. Lett. B **546**, 55 (2002).
[47] J. I. Prisciandaro *et al.*, Nucl. Phys. **A682**, 200c (2001).
[48] S. N. Liddick *et al.*, Phys. Rev. Lett. (to be published).
[49] O. Sorlin *et al.*, Nucl. Phys. **A669**, 351 (2000).
[50] B. H. Flowers and L. D. Skouras, Nucl. Phys. **A136**, 353 (1969).
[51] M. Hannawald *et al.*, Phys. Rev. Lett. **82**, 1391 (1999).
[52] G. Kraus *et al.*, Phys. Rev. Lett. **73**, 1773 (1994).
[53] H. Nakada, T. Sebe, and T. Otsuka, Nucl. Phys. **A571**, 467 (1994).
[54] D. Rudolph *et al.*, Eur. Phys. J. A **4**, 115 (1999).
[55] H. Junde, Nucl. Data Sheets **87**, 507 (1999).
[56] M. Honma *et al.*, in *Proceedings of the International Workshop on Collective Excitations in Fermi and Bose Systems*, edited by C. A. Bertulani *et al.* (World Scientific, Singapore, 1999), p. 468.
[57] H. Junde, Nucl. Data Sheets **68**, 887 (1993); H. Junde, interim evaluation, 1995.
[58] H. Junde, Nucl. Data Sheets **64**, 723 (1991); H. Junde, interim evaluation, 1995.
[59] H. Junde, Nucl. Data Sheets **86**, 315 (1999).
[60] D. Rudolph *et al.*, Phys. Rev. Lett. **82**, 3763 (1999).
[61] M. R. Bhat, Nucl. Data Sheets **85**, 415 (1998).
[62] M. R. Bhat, Nucl. Data Sheets **80**, 789 (1997); B. Singh, interim evaluation, 2001.
[63] C. M. Baglin, Nucl. Data Sheets **69**, 733 (1993).
[64] I. Schneider *et al.*, Phys. Rev. C **61**, 044312 (2000).
[65] H. Junde, Nucl. Data Sheets **68**, 887 (1993); H. Junde and H. Su, interim evaluation, 2001.
[66] A. F. Lisetskiy, R. V. Jolos, N. Pietralla, and P. von Brentano, Phys. Rev. C **60**, 064310 (1999).
[67] B. Singh, Nucl. Data Sheets **87**, 177 (1999); B. Singh, interim evaluation, 2001.
[68] Y. Fujita *et al.*, Eur. Phys. J. A **13**, 411 (2002).
[69] A. F. Lisetskiy *et al.*, Phys. Rev. C **68**, 034316 (2003).
[70] P. von Brentano *et al.*, Nucl. Phys. **A682**, 48c (2001).